International Journal for Numerical Methods in Biomedical Engineering

WILEY

BASIC RESEARCH OPEN ACCESS

Accurate Reconstruction of Right Heart Shape and Motion From Cine-MRI for Image-Driven Computational Hemodynamics

Francesca Renzi[1] | Christian Vergara[2] | Marco Fedele[3] | Vincenzo Giambruno[1] | Alfio Quarteroni[3,4] | Giovanni Puppini[5] | Giovanni Battista Luciani[1]

[1]Dipartimento di Scienze Chirurgiche Odontostomatologiche e Materno-Infantili, Università di Verona, Verona, Italy | [2]LaBS, Dipartimento di Chimica, Materiali e Ingegneria Chimica, Politecnico di Milano, Milan, Italy | [3]MOX, Dipartimento di Matematica, Politecnico di Milano, Milan, Italy | [4]Institute of Mathematics, École Polytechnique Fédérale de Lausanne, Lausanne, Switzerland | [5]Dipartimento di Radiologia, Università di Verona, Verona, Italy

Correspondence: Christian Vergara (christian.vergara@polimi.it)

Received: 16 February 2024 | **Revised:** 26 August 2024 | **Accepted:** 19 November 2024

Keywords: cardiac MRI | computational fluid dynamics | in silico investigation | patient-specific analysis | reconstruction | right heart

ABSTRACT

Accurate reconstruction of the right heart geometry and motion from time-resolved medical images is crucial for diagnostic enhancement and computational analysis of cardiac blood dynamics. Commonly used segmentation and/or reconstruction techniques, exclusively relying on short-axis cine-MRI, lack precision in critical regions of the right heart, such as the ventricular base and the outflow tract, due to its unique morphology and motion. Furthermore, the reconstruction procedure is time-consuming and necessitates significant manual intervention for generating computational domains. This study introduces an end-to-end hybrid reconstruction method specifically designed for computational simulations. Integrating information from various cine-MRI series (short/long-axis and 2/3/4 chambers views) with minimal user contribution, our method leverages registration- and morphing-based algorithms to accurately reconstruct crucial cardiac features and complete cardiac motion. The reconstructed data enable the creation of patient-specific computational fluid dynamics models, facilitating the analysis of the hemodynamics in healthy and clinically relevant scenarios. We assessed the accuracy of our reconstruction method against ground truth and a standard method. We also evaluated volumetric clinical parameters and compared them with the literature values. The method's adaptability was investigated by reducing the number of cine-MRI views, highlighting its robustness with varying imaging data. Numerical findings supported the reliability of the approach for simulating hemodynamics. Combining registration- and morphing-based algorithms, our method offers accurate reconstructions of the right heart chambers' morphology and motion. These reconstructions can serve as valuable tools as domain and boundary conditions for computational fluid dynamics simulations, ensuring seamless and effective analysis.

1 | Introduction

Right ventricular function is affected by a variety of cardiac disease conditions where acute or chronic pressure or volume overload occurs. Among the more common causes of pressure overload are pulmonary hypertension, either primary or secondary to left-sided cardiac valve disease, congenital heart disease, cardiomyopathies, and, less commonly, ischemic heart disease. Chronic volume overload of the right heart (RH) is primarily related to complex congenital heart disease, namely the sequelae of repair of tetralogy of Fallot (ToF) or similar disease conditions, and less commonly to acquired valve disease. Dysfunction of the right ventricle (RV) is linked to elevated cardiac morbidity and mortality [1]. Consequently, the investigation of the RH

function and, specifically, of RH blood dynamics holds paramount importance in clinical practice.

In this context, the three-dimensional morphology and motion of RH and valves can significantly contribute to the reliability of in silico hemodynamic investigations within patient-specific frameworks, which nowadays are widely adopted to address diverse clinical queries. To incorporate the myocardial motion in computational analysis, fluid–structure interaction (FSI) modelling [2–4] can be considered. Alternatively, the cardiac chambers' displacement can be prescribed either from offline electromechanics simulation [5–10] or from imaging preprocessing [11–17]. The availability of time-resolved imaging, such as cine-MRI, allowing the reconstruction of a reliable wall displacement, makes image-driven computational fluid dynamics (ID-CFD) an efficient approach for simulating cardiac blood dynamics. This simplifies the mathematical complexity of FSI and obviates the need for structure parameters calibration and for finding the unloaded configuration, at the expense of a greater effort in the pre-processing phase.

Currently, a few studies have been focused on ID-CFD for the RH [14, 15, 17, 18]. In this context, the accurate replication of the geometry and motion of the RH is crucial, given its challenging reconstruction due to its morphologic complexity [19, 20]. While the ellipsoidal shape of the left heart allows for the use of standard techniques, identifying the unique shape of the RH necessitates ad hoc reconstruction strategies. Moreover, unlike the left heart, which contracts mainly radially, the RH predominantly exhibits motion along the longitudinal direction [21], complicating the identification of the basis between the tricuspid and pulmonary orifices. However, standard reconstruction techniques often rely on short-axis (SA) acquisitions solely [19, 22–25]. Unfortunately, the atrioventricular plane is not explicitly detectable along the SA sections due to the longitudinal contraction, jeopardizing the reconstruction of the RH motion and, in turn, the reliability of ID-CFD results.

To overcome these limitations, promising results have been achieved by merging the information from different types of MR acquisitions in the reconstruction procedure. For instance, SA and long-axis (LA) cine-MRIs of the left ventricle can be merged to obtain reconstructions at two instants (end-diastole and end-systole) [26, 27], or to capture the left ventricular wall motion throughout the whole systolic phase [13]. In addition, another approach can involve the use of MRIs of diverse nature, such as SA and LA cine-MRIs and contrast-enhanced MR angiography (CE-MRI) [14]. Finally, recent techniques based on training suitable neural networks have been proposed to automate the segmentation and reconstruction [28–31].

In this study, we propose a novel method for the reconstruction of RH 3D geometries and motion in view of ID-CFD, which exploits and merges different time-resolved cine-MRI series. This aims at improving the geometrical accuracy beyond what SA images alone can achieve and overcome the limitations of previous studies, particularly by allowing us to avoid the image blurring of points not belonging to the original acquisition planes [13], to avoid more invasive and less routine MR acquisitions (such as CE-MRA [14]), and to obtain the endocardium motion during the whole heartbeat.

The proposed method consists of initial contouring of the endocardium on the cine-MRI slices for a time frame of the cardiac cycle. Subsequently, a deformation of these contours over the heartbeat is achieved, yielding, for each frame, a set of contours covering the whole endocardium. From these sets, we recover the 3D endocardial surface at each frame by morphing a template surface. The 3D vector field representing the endocardial displacement is obtained using a 3D registration algorithm over artificial level-set images of the reconstructed endocardial configurations [32]. Given that the proposed method exploits different cine-MRI series and applies a morphing procedure to generate the reconstructed cardiac volumes and motion, we henceforth refer to it as *Multi-Series Morphing (MSMorph)* technique. We apply the proposed method to a healthy subject and a repaired ToF patient (TF), assessing its accuracy by comparing the results with the original images and with reconstructions obtained with a standard technique.

In the second part of the study, we aim to use the reconstructed geometries and motion of the RH of the two preprocessed cases to perform ID-CFD numerical simulations. We evaluate velocity and pressure fields at different time instants together with a quantification of turbulence development, and we check the significance of the results by a comparison with literature ranges. This allows us to assess the reliability of our preprocessing method given its application to clinical problems where blood dynamics is relevant.

Summarizing, the key contributions of this study are as follows:

- By integrating image registration and morphing-based techniques, our reconstruction approach effectively utilizes differently oriented cine-MRI volumetric series[1] to reconstruct the morphology and motion of the RH. This enables the extraction of through-plane geometry and motion information, which are inaccessible when relying solely on a single cine-MRI view;
- Implemented within a semi-automatic pipeline, our reconstruction method demands minimal user contribution and facilitates the generation of the computational mesh and displacement field of the RH in view of dynamic ID-CFD analysis;
- RH ID-CFD experiments based on the proposed reconstruction technique show significant results in both the healthy and ToF cases.

The rest of the article is organized as follows: in Sections 2 and 3, we describe the reconstruction methods and report the corresponding results, respectively. Then, in Section 4, we introduce the mathematical and numerical model of ID-CFD together with the numerical results in Section 5. We conclude the article in Section 6 with some limitations and discussion of further developments.

2 | Reconstruction of RH Geometry and Motion

In this section, we present the medical images at the disposal (Section 2.1); the proposed method (MSMorph) for the reconstruction of the patient-specific RH comprehensive of the RV,

the right atrium (RA), the pulmonary trunk (PA), and the tricuspid and pulmonary valves (TVs, PVs) (Section 2.2); the process for generating the computational domain for the RH ID-CFD simulations (Section 2.3); and the metrics adopted for the analysis of the reconstruction results (Section 2.4).

2.1 | Clinical Data

A healthy subject (hereafter referred to as H) and a patient with chronic PV insufficiency after repair of ToF in infancy (hereafter referred to as TF) underwent clinically indicated and ad hoc cardiac cine-MRI studies. Specifically, these studies enable the acquisition of the RV, the RA, and the pulmonary artery (PA), as well as the TV and PV.

Cardiac cine-MRI data were provided by the Division of Radiology, University Hospital Verona, Verona, Italy. The acquisitions were performed using Achieva 1.5T (TX)–DS (Philips, Amsterdam, the Netherlands) technology and consist of slices with homogeneous in-plane spatial resolution ranging from 1.15 to 1.25 mm and thickness ranging from 5 to 8 mm. The datasets include some or all of the following:

- SA cine-MRI: volumetric series made up of 15 to 21 slices stacked along the RV main axis direction and including both RA and RV;
- LA cine-MRI: volumetric series made up of six slices stacked along the direction orthogonal to the RV main axis;
- SA aortic valve (AV-SA) cine-MRI: volumetric series made up of six slices stacked along the direction normal to the aortic valve plane;
- 2D series of LA cine-MRI acquired on two-chambers (2 Ch), three-chambers (3 Ch), and four-chambers (4 Ch) planes;
- Rotational TV (TV-R) cine-MRI: volumetric series of 18 evenly rotated planes around the axis connecting the center of the TV orifice to the RV apex.

All series have a time resolution of 30 frames/cardiac cycle. AV-SA cine-MRI and TV-R cine-MRI are specific acquisitions designed to capture the cross-sectional shape of the Valsalva's sinuses and the 3D evolution of the TV annulus, respectively. Refer to Figure 1 for a detailed representation of some of such acquisitions.

2.2 | Methods for Preprocessing: The MSMorph Procedure

Our reconstruction method needs both SA cine-MRI and LA cine-MRI to be implemented. AV-SA, 2 Ch, 3 Ch, 4 Ch, TV-R cine-MRI could be added to the procedure to improve the accuracy. The method is subdivided into three steps:

1. Generation of the contours representing the endocardial surface using the cine-MR acquisitions at disposal (Section 2.2.1);
2. Generation of the endocardial surface (Section 2.2.2);
3. Definition of the endocardial displacement field (Section 2.2.3).

We highlight that the steps above represent the new contributions of this study. Moreover, this pipeline allows the separate reconstruction of both the RV endocardial surface and the RA endocardial surface.

The entire procedure, outlined in Figure 2, is carried out using the open-source software 3D Slicer (https://www.slicer.org/),

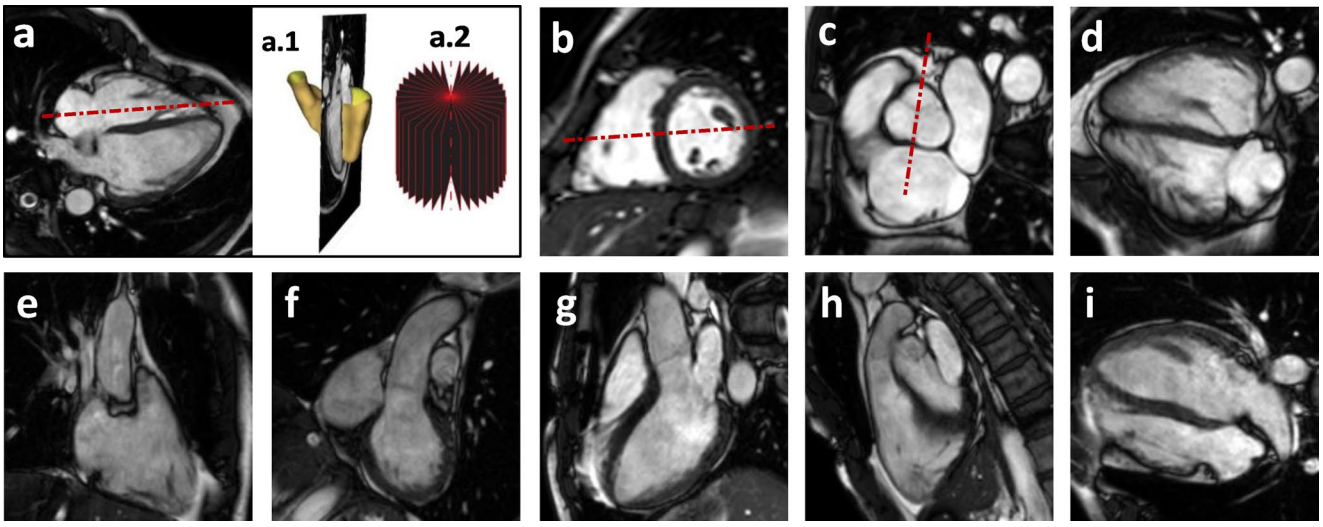

FIGURE 1 | The first row lists the volumetric cine-MRI series with the corresponding cardiac MRI planes: (a) 2D view of a rotational long axis plane, (a.1) 3D view of the same rotational plane over the reconstructed right ventricles surface, (a.2) scheme of the 18 rotational planes; (b) short axis plane; (c) aortic valve short axis plane; (d) long axis plane. The second row lists the set of 2D long-axis cine-MRI: (e) specific view for the right heart evaluation; (f) specific view where the left ventricle, the right atrium, and the aortic root are visible; (g) specific view for the evaluation of the aortic flow; (h) three chambers plane where the pulmonary flow is visible; (i) four chambers view.

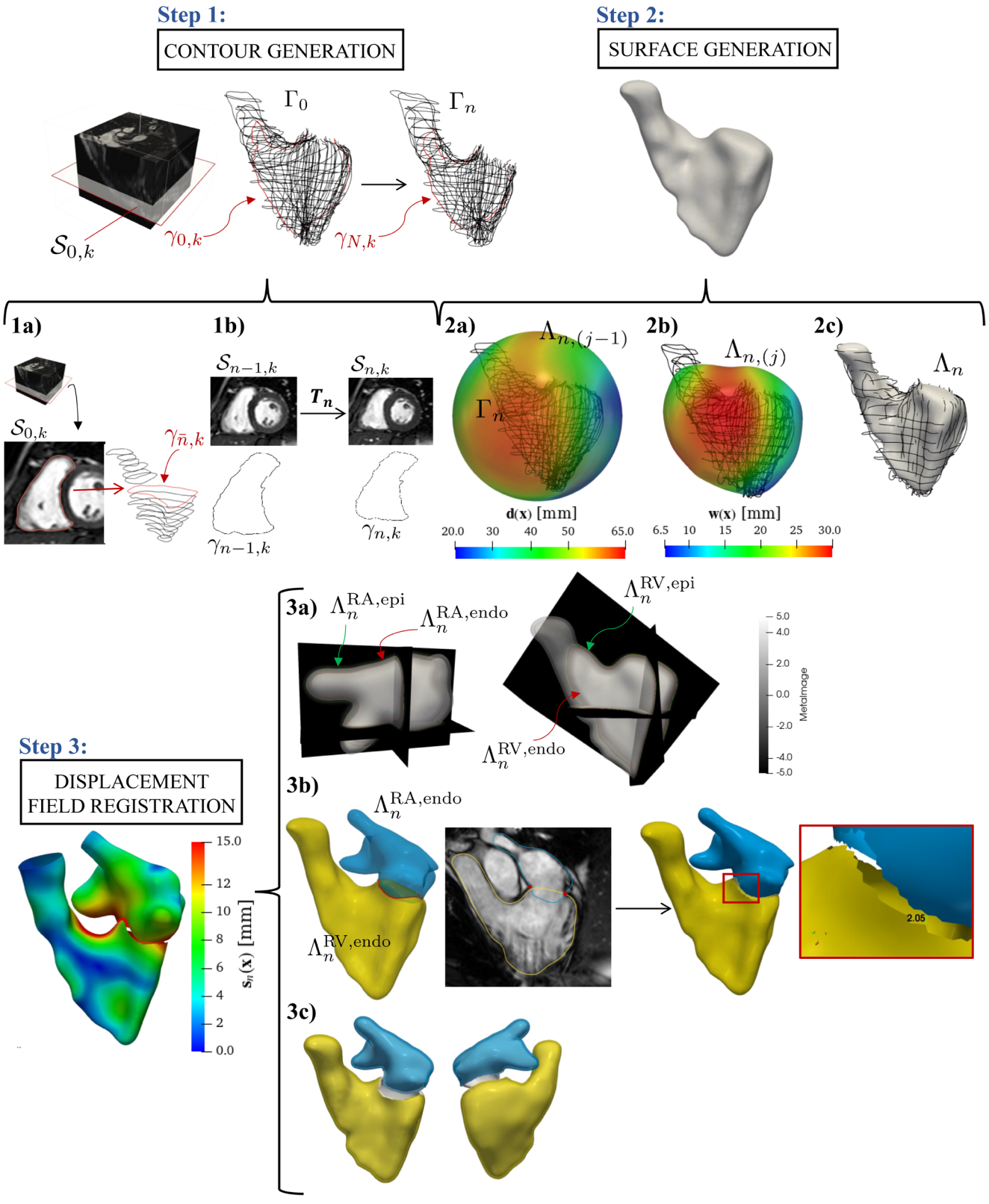

FIGURE 2 | Legend on next page.

the Vascular Modeling Toolkit (`vmtk`, http://www.vmtk.org/ [33]), enriched by additional tools for the cardiac surface processing [34], and the SimpleElastix library for image registration (https://simpleelastix.github.io/ [35]). Finally, the reconstruction results are analyzed with ParaView (https://www.paraview.org) visualization software.

2.2.1 | Step 1: Contour Generation by a semi-automatic 2D Registration

In what follows, we detail the semi-automatic procedure introduced in this study for contour generation, which relies on non-rigid registration (see Figure 2—Step 1). Let k denote the

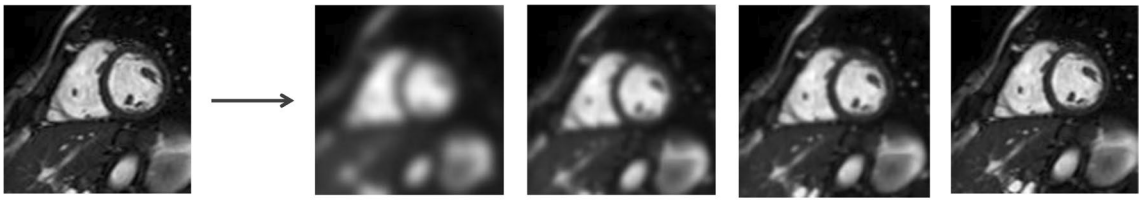

FIGURE 3 | Multi-resolution strategy using the Gaussian filtering with kernel size equal to 21×21, 11×11, 7×7, and 5×5 pixels. These sizes are obtained by imposing an image shrinking factor of 8, 4, 2, 1 in the procedure proposed by the SimpleElastix library [35] and based on the image spacing. No down-sampling is applied. The original $\mathcal{S}_{n,k}$ on the left side of the arrow. On the right side, the filtered $\mathcal{S}_{n,k}$ at each resolution level.

index spanning the total slice number of the cine-MRI series available (inclusive of both SA and LA and, potentially, other cine-MRI acquisitions, as shown in Figure 1). Let $t_n = n\tau_{\text{cMRI}}$, where $n = 0, \ldots, N = T/\tau_{\text{cMRI}}$, represent the acquisition times of the cine-MRI. Here, τ_{cMRI} denotes the time resolution of the cine-MRI, and T is the heartbeat duration. For each physical slice $\Omega_{n,k} \subset \mathbb{R}^2$, the grey-level function $\mathcal{S}_{n,k}$ is available from the MRI acquisitions, allowing us to trace the endocardial contours $\gamma_{n,k}$, grouped at each t_n in the sets Γ_n.

First, we generate an initial set $\Gamma_{\overline{n}}$ by selecting $\overline{n}$ as the onset of the diastasis phase, a stage of the diastole immediately before the atrial contraction that corresponds to intermediate atrial and ventricular volumes. To construct $\gamma_{\overline{n},k}$, the endocardium is manually outlined in each slice of the available cine-MRI series by placing markup points which are then interpolated using Kochanek splines. This process is accomplished using the *Markups* module in the 3D Slicer software (see Figure 2—Step 1a). Our proposal is now to obtain the remaining sets Γ_n without manual tracing but through the deformation of $\Gamma_{\overline{n}}$ both forward and backward in time. This is realized by means of a non-rigid registration algorithm applied to time-consecutive image slices, and implemented in the open-source registration library SimpleElastix. The representation of this idea is sketched in Figure 2—Step 1b.

In particular, for each k, we search for the 2D transformation maps $T_{n,k}$:

$$\boldsymbol{T}_{n,k} = \begin{cases} \boldsymbol{T}^F_{n,k} : \Omega_{n,k} \to \Omega_{n+1,k} & \forall n = \overline{n}, \ldots, N-1 \\ \boldsymbol{T}^B_{n,k} : \Omega_{\overline{n}-n,k} \to \Omega_{\overline{n}-n-1,k} & \forall n = 0, \ldots, \overline{n}-1, \end{cases} \tag{1}$$

where $\boldsymbol{T}^F_{n,k}$ and $\boldsymbol{T}^B_{n,k}$ spatially align the grey-level function $\mathcal{S}_{n,k}$ with $\mathcal{S}_{n+1,k}$ and $\mathcal{S}_{n-1,k}$, respectively.

Among others, we consider a non-rigid transformation $\boldsymbol{T}_{n,k}$ based on B-spline to account for the large deformations involved in the myocardial contraction. The registration problem traduces into the minimization of a cost functional w.r.t. $\boldsymbol{T}_{n,k}$. This functional comprises a similarity measure based on mutual information, as defined in [36], and a smoothness constraint that penalizes sharp deviations of the transformation [37]. We found the standard gradient descent to be a suitable optimizer for this minimization problem. In particular, the registration is performed with a multi-resolution strategy [38] with four resolution levels. At each level, we apply a Gaussian filter to $\mathcal{S}_{n,k}$ without down-sampling with a variable kernel. This helps to manage the complexity of the transformation while preventing entrapment into local minima. In Figure 3, we show the result of applying the Gaussian filter without down-sampling to $\mathcal{S}_{n,k}$ at the four resolution levels. As expected, the quality of the image progressively increases. In addition, the absence of down-sampling avoids the introduction of artifacts. Finally, we notice that, at each resolution level, the minimization process is stopped after 500 iterations of the standard gradient descent method.

The output of the registration procedure is the transformation $\boldsymbol{T}_{n,k}$ which transforms $\gamma_{n,k}$ in the time-subsequent configuration $\gamma_{n+1,k}$ (or the previous configuration $\gamma_{n-1,k}$) (see Figure 2—Step 1b). For each t_n, the ensemble of all $\gamma_{n,k}$ generated by the registration procedure gives rise to the contour set Γ_n, which serves as our starting point to define the endocardial surface in the next section.

2.2.2 | Step 2: Surface Generation by Morphing

In this section, we describe our procedure for the generation of the 3D endocardial surface from the contour sets Γ_n (Figure 2—Step 2) created at the previous step. In particular, this is

FIGURE 2 | Overall reconstruction procedure. Step 1: Endocardial contours generation from cine-MRI. Zoom on Step 1 (Section 2.2.1): (1a): manual tracing of the endocardial border (dotted red line on slice $\mathcal{S}_{\overline{n},k}$) on every cine-MRI slice for a fixed time frame; (1b): sketch of the non-rigid registration algorithm applied to time consecutive slices and deformation of the endocardial contour due to the application of the resulting transformation. Step 2: Morphing procedure. Zoom on Step 2 (Section 2.2.2): (2a): extended and smoothed distance field $\boldsymbol{d}(\boldsymbol{x})$ defined on the template surface $\Lambda_{n,(j-1)}$, superimposed on the contours set Γ_n (Section 2.2.2—[i], [ii], [iii]); (2b): representation of the vector field $\boldsymbol{w}(\boldsymbol{x})$ defined as in Section 2.2.2—[iv] on the warped template surface $\Lambda_{n,(j)}$; (2c): resulting surface at frame n. Step 3: recovery of the endocardial displacement field and representation of the displacement field $\boldsymbol{s}_n(\boldsymbol{x})$ on the reference configurations of RA and RV at the end-systolic instant. Zoom on Step 3 (Section 2.2.3): (3a): endocardial and epicardial faces of RA ($\Lambda_n^{\text{RA,endo}}$, $\Lambda_n^{\text{RA,epi}}$) and RV ($\Lambda_n^{\text{RV,endo}}$, $\Lambda_n^{\text{RV,epi}}$) superimposed on the level set images of the RA and RV endocardial surfaces; (3b): a sketch of the TV orifice definition as the intersection between the atrial and ventricular endocardial reconstructions (blue and yellow surfaces respectively on the left) and visualization on a representative TV-R cine-MRI slice of the intersecting points (red dots); zoom of the TV annular gap (right); (3c): representation of the false myocardium of RV and RA.

realized by morphing a template surface Σ (independent of n, see Figure 2—Step 2a), suitably chosen by the user[2].

At each time t_n, we proceed as follows:

Set $\Lambda_{n,(0)} = \Sigma$ and for each $j = 1, \ldots$:

i. Compute the distance field $\boldsymbol{g}_{n,(j)}(\boldsymbol{x})$ between Γ_n and $\Lambda_{n,(j-1)}$ defined on $\Theta_{n,(j-1)} = \{\boldsymbol{x} \in \Lambda_{n,(j-1)}\colon\ \boldsymbol{x} = \text{argmin}_{\boldsymbol{y}} \| \boldsymbol{y} - \hat{\boldsymbol{x}} \|_{\mathbb{R}^3}, \forall \hat{\boldsymbol{x}} \in \Gamma_n\}$;

ii. Extend the distance field $\boldsymbol{g}_{n,(j)}$ over the whole surface $\Lambda_{n,(j-1)}$[3] by solving the vectorial Laplace-Beltrami problem:

$$\begin{cases} -\Delta_\Lambda \boldsymbol{d}_{n,(j)} = 0 & \text{in } \Lambda_{n,(j-1)}, \\ \boldsymbol{d}_{n,(j)} = \boldsymbol{g}_{n,(j)} & \text{on } \Theta_{n,(j-1)}; \end{cases} \tag{2}$$

iii. Smooth the field $\boldsymbol{d}_{n,(j)}$ using a moving average filter, where, at the finite elements level, for each node of the surface mesh, the width is given by its element patch (the resulting smoothed field is reported in Figure 1—Step 2a);

iv. Deform the surface $\Lambda_{n,(j-1)}$ according to the vector field $\boldsymbol{w}_{n,(j)} = C\boldsymbol{d}_{n,(j)}$, where C is a user-defined scaling factor, obtaining

$$\Lambda_{n,(j)} = \{\boldsymbol{x} = \boldsymbol{y} - \boldsymbol{w}_{n,(j)}(\boldsymbol{y}),\ \ \forall \boldsymbol{y} \in \Lambda_{n,(j-1)}\}$$

(see Figure 2—Step 2b);

v. Remesh the surface $\Lambda_{n,(j)}$;

vi. Check the stopping criterion: if $\| \boldsymbol{w}_{n,(j)} \| < \varepsilon$, then set $\Lambda_n = \Lambda_{n,(j)}$ (see Figure 22c) and $n \to n+1$; else $j \to j+1$.

Refer to Algorithm 1. In this study, empirical evidence suggested that maintaining a constant value for the scaling factor C achieved a uniform distribution of $\boldsymbol{w}_n$; specifically, we used $C = 0.5$ for this purpose. Notice that the deformation Σ in an iterative fashion, rather than in just one step by its initial distance to Γ_n, and the presence of a remeshing step after deformation (Step v) allow us to avoid issues of mesh entanglements/interpenetration or element distortions that would have occurred otherwise. Moreover, this algorithm is adept at merging and filtering the information from various cine-MRIs.

ALGORITHM 1 | Surface Generation by Morphing.

for $0 \le n < N$ **do**
Set $\Lambda_{n,(0)} = \Sigma$ and define
$\Theta_{n,(0)} = \{\boldsymbol{x} \in \Lambda_{n,(0)}\colon\ \boldsymbol{x} = \text{argmin}_{\boldsymbol{y}} \| \boldsymbol{y} - \hat{\boldsymbol{x}} \|_{\mathbb{R}^3}, \forall \hat{\boldsymbol{x}} \in \Gamma_n\}$
for $j = 1, \ldots$ **do**:
Compute $\boldsymbol{g}_{n,(j)}$;
Extend $\boldsymbol{g}_{n,(j)}$ over $\Lambda_{n,(j-1)}$, solving:

$$\begin{cases} -\Delta_\Lambda \boldsymbol{d}_{n,(j)} = 0 & \text{in } \Lambda_{n,(j-1)}, \\ \boldsymbol{d}_{n,(j)} = \boldsymbol{g}_{n,(j)} & \text{on } \Theta_{n,(j-1)}; \end{cases}$$

Smooth $\boldsymbol{d}_{n,(j)}$ by means of a moving average filter;
Deform $\Lambda_{n,(j-1)}$ according to $\boldsymbol{w}_{n,(j)} = C\boldsymbol{d}_{n,(j)}$:
$\Lambda_{n,(j)} = \{\boldsymbol{x} = \boldsymbol{y} - \boldsymbol{w}_{n,(j)}(\boldsymbol{y}),\ \ \forall \boldsymbol{y} \in \Lambda_{n,(j-1)}\}$;
Remesh $\Lambda_{n,(j)}$;
if $\| \boldsymbol{w}_{n,(j)} \| < \varepsilon$ **then**
set $\Lambda_n = \Lambda_{n,(j)}$;

$$n \to n+1;$$

else

$$j \to j+1.$$

end if
end for
end for

2.2.3 | Step 3: Displacement Recovery

We aim at registering the reconstructed surfaces Λ_n to generate the vector fields $s_n(x)$ (Figure 2—Step 3) that describe endocardial displacements w.r.t. a reference configuration throughout the entire heartbeat. To accomplish this, we adapt the method developed in [32], based on a non-rigid registration among artificial level-set images. Moreover, we exploit the generation of thick closed surfaces of the RA and RV that we call *tentative myocardial* surfaces. We stress that generating such surfaces serves the sole purpose of obtaining closed surfaces to aid the creation of the artificial level-set images needed to recover the RA and RV endocardial displacement fields. These surfaces are not meant to replicate the patient's actual myocardium.

The complete pipeline, outlined in Figure 2—Step 3, includes the following steps at each n:

i. Generation of endocardial and epicardial surfaces starting from Λ_n;

ii. Definition of the TV orifice (Figure 2—Step 3a) and generation of *tentative myocardial* surfaces for the RA and RV chambers;

iii. Generation of artificial level-set images of the *tentative myocardial* surfaces obtained at Step (ii);

iv. Definition of a reference configuration and application of a multi-resolution registration algorithm based on B-spline transformation among the level-set images generated at Step (iii);

v. Application of the transformation resulting from Step (iv) to the reference configuration.

In Step (i), we generate the level-set images of Λ_n^{RA} and Λ_n^{RV}, which were previously obtained through the morphing algorithm (Section 2.2.2) for RA and RV, respectively, by applying the signed-distance transform. Then, exploiting the marching cube algorithm [39], we extract the level set surfaces of levels 0 and $-t$, where t is a suitable constant equal to 2 mm in this study. We call endocardial the level-0 surfaces, and epicardial the level-t

ones since they are external to the former (see $\Lambda_n^{\mathrm{RA,endo}}$, $\Lambda_n^{\mathrm{RA,epi}}$, $\Lambda_n^{\mathrm{RV,endo}}$, and $\Lambda_n^{\mathrm{RV,epi}}$ in Figure 23a).

In Step (ii), we create the TV orifice on both endocardial and epicardial sides by removing the overlapped region between $\Lambda_n^{\mathrm{RA,endo/epi}}$ and $\Lambda_n^{\mathrm{RV,endo/epi}}$ (see Figure 23b). Finally, we connect the endocardial and the epicardial surfaces at the level of the realized TV orifices, generating new closed and thick surfaces for the atrial and ventricular chambers individually, which we refer to as *tentative myocardial* surfaces (see Figure 23c).

In Step (iii), we build level-set images associated with the *tentative myocardial* surfaces generated above, with a homogeneous space resolution of 1 mm along each direction.

It is worth mentioning that the use of separate RA and RV *tentative myocardial* surfaces allows to fulfill two main requirements. First, we aim at reconstructing the motion of the TV annulus along the cardiac cycle. This point forces the creation of a TV orifice on the RA and RV surfaces before registering their level-set images. Second, we want to avoid the presence of arti facts in such level-set images that would arise when generating them from open surfaces and that, ultimately, would jeopardize the registration.

In Step (iv), after selecting a frame $\hat{n}^4 \in [0, N]$ as reference (e.g., the end-systolic frame), we register these level-set images w.r.t. it. Namely, a multi-resolution non-rigid B-spline-based registration is adopted, with four values of the grid-spacing varying from 22.4 to 8.0 mm. Here, too, a Gaussian smoothing filter without down-sampling is applied. The resulting transformation is the one that maximizes the mutual information between the reference level-set image and the other level-set images, constrained in the bending energy. To do this, an adaptive stochastic gradient descent optimizer is adopted.

In Step (v), the registration transformations are evaluated on the points of the reference endocardial surface $\widehat{\Lambda}^{\ell,\mathrm{endo}}$, $\ell = \mathrm{RA}, \mathrm{RV}$. Hence, we can compute at each n the 3D vector field $\boldsymbol{s}_n^{\ell}(\widehat{\boldsymbol{x}})$ representing the displacement of the endocardium during the heartbeat w.r.t. $\widehat{\Lambda}^{\ell,\mathrm{endo}}$. In the following sections, we denote $\tilde{\Lambda}_n$ as the application of $\boldsymbol{s}_n^{\ell}(\widehat{\boldsymbol{x}})$ to the end-systolic reference configuration $\widehat{\Lambda}^{\ell,\mathrm{endo}}$:

$$\tilde{\Lambda}_n^{\ell} = \left\{ \boldsymbol{x} = \hat{\boldsymbol{y}} - \boldsymbol{s}_n^{\ell}(\hat{\boldsymbol{y}}), \forall \hat{\boldsymbol{y}} \in \widehat{\Lambda}^{\ell,\mathrm{endo}} \right\}, \quad \text{with} \quad n = 0, \ldots, N, \ell = \mathrm{RA}, \mathrm{RV}. \tag{3}$$

Note that Steps (iii), (iv), and (v) of this pipeline are repeated identically for the RA and RV and are inspired by [32], whereas Steps (i) and (ii) are completely new.

Hereafter, we refer to the new reconstruction procedure proposed in this study as the Multi-Series Morphing (MSMorph) technique.

Remark 1. Notice that, when MRI allows it, the MSMorph technique described in Sections 2.2.1, 2.2.2, and 2.2.3 for the endocardial surfaces could be applied to valves' leaflets as well. In this work, imaging allowed us to trace the contours of the pulmonary and TV' leaflets of both subjects only at the end-systolic and end-diastolic configurations in the LA and AV-SA cine-MRI. Thus, in practice, we were able to apply to the two valves only the morphing procedure described in Section 2.2.2. To this aim, we used as a starting template the PV and TV valves from the Zygote solid 3D heart model (https://www.zygote.com/).

2.3 | Generation of the Computational Domain

The computational domain in view of the ID-CFD simulations (see Sections 4 and 5) is built only for the reference configuration of the RH (e.g., at end-systole). To generate the whole RH surface, we connect the reference endocardial surfaces $\widehat{\Lambda}^{\mathrm{RA,endo}}$ and $\widehat{\Lambda}^{\mathrm{RV,endo}}$ (see Section 2.2.2) at the TV annulus. It is important to note that, for the PA, we truncate the computational domain before the bifurcation due to insufficient image clarity for identification. Similarly, flow extensions at the inferior vena cava (IVC) for both subjects are added for the same reason. To recover the continuous displacement field $\boldsymbol{s}_n$ of the complete RH surface, the displacement fields $\boldsymbol{s}_n^{\mathrm{RA}}$ and $\boldsymbol{s}_n^{\mathrm{RV}}$, reconstructed for the ventricular and atrial endocardia (see Section 2.2.3), are harmonically extended to the TV annulus and flow extensions [34]. We complete the RH geometry by including TV and PV, reconstructed from the available cine-MRI using the procedure described in Section 2.2.2 (see Remark 1). In particular, for both valves, we reconstruct the closed and open configurations corresponding to the end-systolic and end-diastolic frames, locating them based on images by extracting the attachment points of the leaflets to the TV orifice and RVOT, respectively.

This reference surface of RH together with its valves defines our computational domain in the reference configuration $\widehat{\Omega}$ (see Figure 4a). Here, Γ_{TV} and Γ_{PV} are the surfaces representing the TV and PV's leaflets, respectively. By Σ_w, we denote the boundary comprising the ventricular and atrial endocardium and the PA, IVC, and SVC walls. Σ_{out} denotes the outlet section of the PA, while Σ_{in} designates the inlet sections of IVC and SVC.

2.4 | Assessment of Reconstruction Results

Since we want to replicate real scenarios coming from data available from hospitals, we consider virtual scenarios, where one has at its disposal different sets of cine-MRI series. Indeed, a complete set of images, such as that described in Section 2.1, is not always routinely acquired in clinical practice and often requires specific acquisitions. Thus, we propose three scenarios: the first one with the complete set of images at disposal, the second where we omit the TV-R cine-MRI series since it often requires ad hoc procedures, and the last where AV-SA cine-MRI series is also neglected for the same reason. Accordingly, in this study, three distinct sets of cine-MRI acquisition series are considered as the input data for the proposed reconstruction method:

- MSMorph-I: all available cine-MRI (SA, LA, AV-SA, 2 Ch, 3 Ch, 4 Ch, TV-R);
- MSMorph-II: all available cine-MRI apart TV-R;

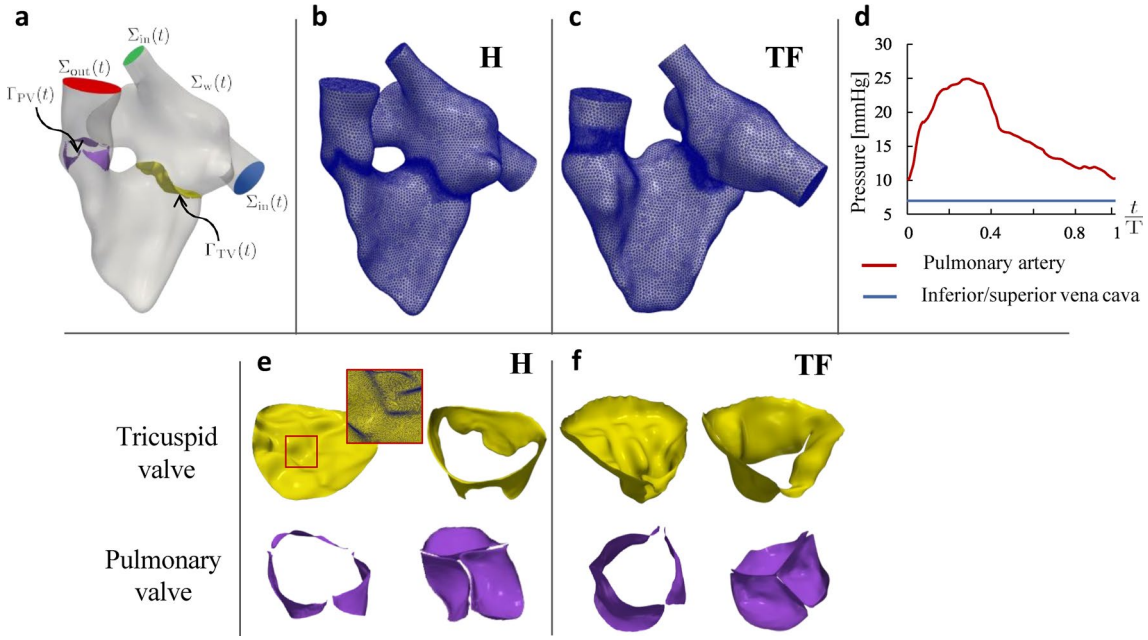

FIGURE 4 | Computational domain and boundary conditions. (a): Representation of the whole right heart $\Omega(t)$ with its boundaries: Ventricle outflow $\Sigma_{out}(t)$; atrial inflows at the superior (green) and inferior (blue) vena cavae $\Sigma_{in}(t)$; ventricular and atrial endocardium and physical wall of the pulmonary artery Σ_w; surface of the pulmonary valve's leaflets $\Gamma_{PV}(t)$; surface of the TV's leaflets $\Gamma_{TV}(t)$. (b, c): Tetrahedric volumetric mesh of the RH of the healthy subject and of the ToF patient. (d): Pressure curves at the pulmonary artery and inferior and superior Vena cavae, imposed as boundary conditions; values come from literature [40, 41]. (e, f): TV and PV in open and closed configurations of the healthy subject and of the ToF patient; red square: detail of the tetrahedral mesh of the healthy TV.

- VMSMorph-III: only SA and LA cine-MRI.

The introduction of variants of the proposed method is meant to explore its robustness with respect to the available amount of information. This allows us to recover, in the MSMorph-III variant, a clinical scenario where TV-R and AV-SA series are not required by the guidelines.

Moreover, following standard techniques introduced so far in the literature, we also consider a reconstruction procedure obtained by using SA images exclusively, referred to hereafter as the SA-based procedure. In particular, among such techniques, we consider the technique proposed in [32], which shares with MSMorph similar procedures for the Steps (iii), (iv), and (v) of Section 2.2.3.

In what follows, we introduce the metrics used for analyzing the accuracy and robustness of the reconstructions obtained with the proposed MSMorph procedure. In the absence of an appropriate ground truth geometry and motion reconstructions, we assess the accuracy of the four aforementioned techniques (the three MSMorph variants and the SA-based procedure) by comparing their results with manually traced contours $\tilde{\Gamma}_n$, obtained by outlining the endocardium in all the available cine-MRI slices and used as the reference solution.

2.4.1 | Assessment of the Discrepancies Introduced by the MSMorph Steps

In this paragraph, we aim at investigating how the main three steps of the MSMorph procedure—namely contours generation (Section 2.2.1), surface generation (Section 2.2.2), and wall displacement registration (Section 2.2.3)—contribute to the overall discrepancy. For this purpose, we consider: the reconstructed contours set Γ_n, outcome of the contour generation step; the surfaces Λ_n^{endo}, outcome of the morphing-based surface generation step; the reconstructed surfaces $\tilde{\Lambda}_n$, outcome of the wall displacement registration step. We introduce the following metrics:

- the Hausdorff Distance $\mathrm{HD}(\tilde{\Gamma}_n, \Gamma_n)$ between the reference solution $\tilde{\Gamma}_n$ and the contours sets Γ_n, defined as:

$$\mathrm{HD} = \max\left\{ \boldsymbol{x}\tilde{\Gamma}_n \sup \inf_{\boldsymbol{y}\in\Gamma_n} \| \boldsymbol{x}-\boldsymbol{y} \|, \sup_{\boldsymbol{x}\in\Gamma_n} \boldsymbol{y}\tilde{\Gamma}_n \inf \| \boldsymbol{x}-\boldsymbol{y} \| \right\}; \tag{4}$$

- the mean squared distance (MSD) between the reference solution $\tilde{\Gamma}_n$ and the contours set Γ_n:

$$\mathrm{MSD} = \sqrt{\frac{1}{|\tilde{\Gamma}_n|}\int_{\tilde{\Gamma}_n} \| \boldsymbol{x}-\overline{\boldsymbol{x}} \|^2_{\mathbb{R}^3}\, d\boldsymbol{x}}, \tag{5}$$

where, given $\boldsymbol{x} \in \tilde{\Gamma}_n$, we define $\overline{\boldsymbol{x}} = \mathrm{argmin}_{\boldsymbol{y}\in\Gamma_n} \| \boldsymbol{y}-\boldsymbol{x} \|_{\mathbb{R}^3}$;

- the $\mathrm{TAMSD}(\tilde{\Gamma}_n, \Lambda_n^{endo})$, between the reference solution $\tilde{\Gamma}_n$ and the reconstructed surface Λ_n^{endo}, defined as follows:

$$\mathrm{TAMSD}(\tilde{\Gamma}_n, \Lambda_n^{endo}) = \sqrt{\frac{1}{T}\sum_{n=0}^{T/\tau_{cMRI}} \frac{1}{|\tilde{\Gamma}_n|}\int_{\tilde{\Gamma}_n} \| \boldsymbol{x}-\overline{\boldsymbol{x}} \|^2_{\mathbb{R}^3}\, d\boldsymbol{x}}, \tag{6}$$

where, given $\boldsymbol{x} \in \tilde{\Gamma}_n$, we define $\overline{\boldsymbol{x}} = \mathrm{argmin}_{\boldsymbol{y}\in\Lambda_n^{endo}} \| \boldsymbol{y}-\boldsymbol{x} \|_{\mathbb{R}^3}$.

- the TAMSD$\left(\Lambda_n^{\text{endo}}, \tilde{\Lambda}_n\right)$, obtained by an expression analogous to Equation (6).

2.4.2 | Assessment of the Overall Reconstruction Accuracy

The overall discrepancy between the reconstructed endocardial surface $\tilde{\Lambda}_n$ (obtained in Section 2.2.3—Step v) and the reference solution $\tilde{\Gamma}_n$ is quantified by computing the following metrics:

• the time average MSD, TAMSD$\left(\tilde{\Gamma}_n, \tilde{\Lambda}_n\right)$, obtained by an expression analogous to Equation (6);

• the Hausdorff Distance HD$\left(\tilde{\Gamma}_n, \tilde{\Lambda}_n\right)$, obtained by an expression analogous to Equation (4).

We also quantify the metric α_n, which is a global indicator of the geometric difference between MSMorph-II, MSMorph-III, and SA-based w.r.t. the more informed technique MSMorph-I:

$$\alpha_n(\boldsymbol{x}) = |\, \boldsymbol{G}_0(\boldsymbol{x}) \,| + |\, \boldsymbol{s}_n^{\text{diff}} \,| \tag{7}$$

where the first contribution represents the discrepancy of the initial reconstruction computed as the 3D displacement needed to map the reconstructed geometries obtained by MSMorph-II, MSMorph-III, or SA-based onto that obtained by MSMorph-I at the reference end-systolic configuration. The second contribution represents the difference between the reconstructed displacements at instant t_n.

The ethical review board approval and informed consent were obtained from all patients.

3 | Reconstruction Procedure: Results and Discussion

We start in Section 3.1 by presenting the reconstruction results of the RV of the healthy subject (H), obtained by applying the three variants MSMorph-I, MSMorph-II, and MSMorph-III of the new procedure introduced in this study. These reconstructions are also compared with those obtained by the SA-based technique, which exploits only the SA cine-MRI, reported here as an example of a reconstruction procedure commonly used by the researchers active in the field. In Section 3.2, we present the reconstruction results of the right atria of H, obtained by our procedures. In Section 3.3, we investigate how the main three steps, described in Sections 2.2.1, 2.2.2, 2.2.3, of the MSMorph procedure contribute to the overall discrepancy between the reconstructed endocardial surfaces and the reference solution. In Section 3.4, we present the results of the whole RH reconstruction of the repaired TF. Finally, in Section 3.5, we provide a brief discussion of the results.

3.1 | Comparison of RV Reconstructions

In this section, we compare the RV and PA reconstructions obtained through three MSMorph procedures and the SA-based technique. Our focus is on subject H, and we refer to the MSMorph definitions outlined at the beginning of Section 2.4. Specifically, the available acquisition series include SA, LA, AV-SA, and TV-R cine-MRI.

In Figure 5, we present the end-systolic reconstructions (left column) and end-diastolic reconstructions together with the normal component of the end-diastolic displacement $\boldsymbol{s}_n$ (central column). This choice is driven by noticing that the overall displacement magnitude contains tangential components that are not unique when registering surfaces. Further, the normal component allows us to distinguish among displacements happening along and against the surface normal. We observe that MSMorph-I yields the smoothest RV endocardial surfaces, offering enhanced clarity in identifying the pulmonary sinuses. The surface irregularities in the reconstructions obtained by MSMorph-II and, most remarkably, by MSMorph-III are attributed to the less informative wealth of images used compared with MSMorph-I. Values of discrepancies w.r.t. the reference solution TAMSD$\left(\tilde{\Gamma}_n, \tilde{\Lambda}_n\right)$, reported in Table 1, confirm this trend. Looking at the central column of Figure 5, we observe that the three MSMorph reconstructions share a similar distribution of the normal displacement over the surface. In contrast, the SA-based reconstruction exhibits a lower normal displacement of the ventricular base and a more pronounced outward normal displacement at the level of the apex and the interventricular septum. The right column of Figure 5 depicts the spatial distribution of the quantity α_n, representing the discrepancies w.r.t. MSMorph-I reconstruction. As expected, MSMorph-III features the largest discrepancies, particularly in the region of RVOT.

To compare the MSMorph strategy with the literature, where only SA cine-MRI series are used for RV geometric reconstruction, we present in Figure 5 the reconstructions obtained with the SA-based technique. On analyzing the values of TAMSD$\left(\tilde{\Gamma}_n, \tilde{\Lambda}_n\right)$ (Table 1), it is evident that the RV endocardial surfaces generated with the SA-based method are less in accordance with the reference solution compared with the MSMorph ones. Visually, in the left column of Figure 5, notable differences are observed, primarily at the base and of the outflow tract (RVOT). Therefore, in such regions, the parameter α_n reaches values of approximately 1.5 cm. Table 1 confirms that, unlike the MSMorph methods, the SA-based method features significant errors for the ventricle w.r.t. the reference solution.

Considering the evolution of RV volume over the cardiac cycle, we note from Figure 5, top right, that there is a strong overlap between the volumes obtained with MSMorph-II and MSMorph-III, whereas slight differences are noticed for MSMorph-I results. More remarkably, substantial differences are noted between MSMorph and SA-based RV volumes, amounting to almost 20% throughout the whole heartbeat. The latter is also characterized by more pronounced fluctuations compared with MSMorph.

In summary, the reported results indicate that the SA-based procedure leads to less accurate reconstructions of the RV compared with the MSMorph approach. This is evident in terms of the distance from the reference solution and in terms of the low RV volume, attributed to the less detailed reconstruction of the

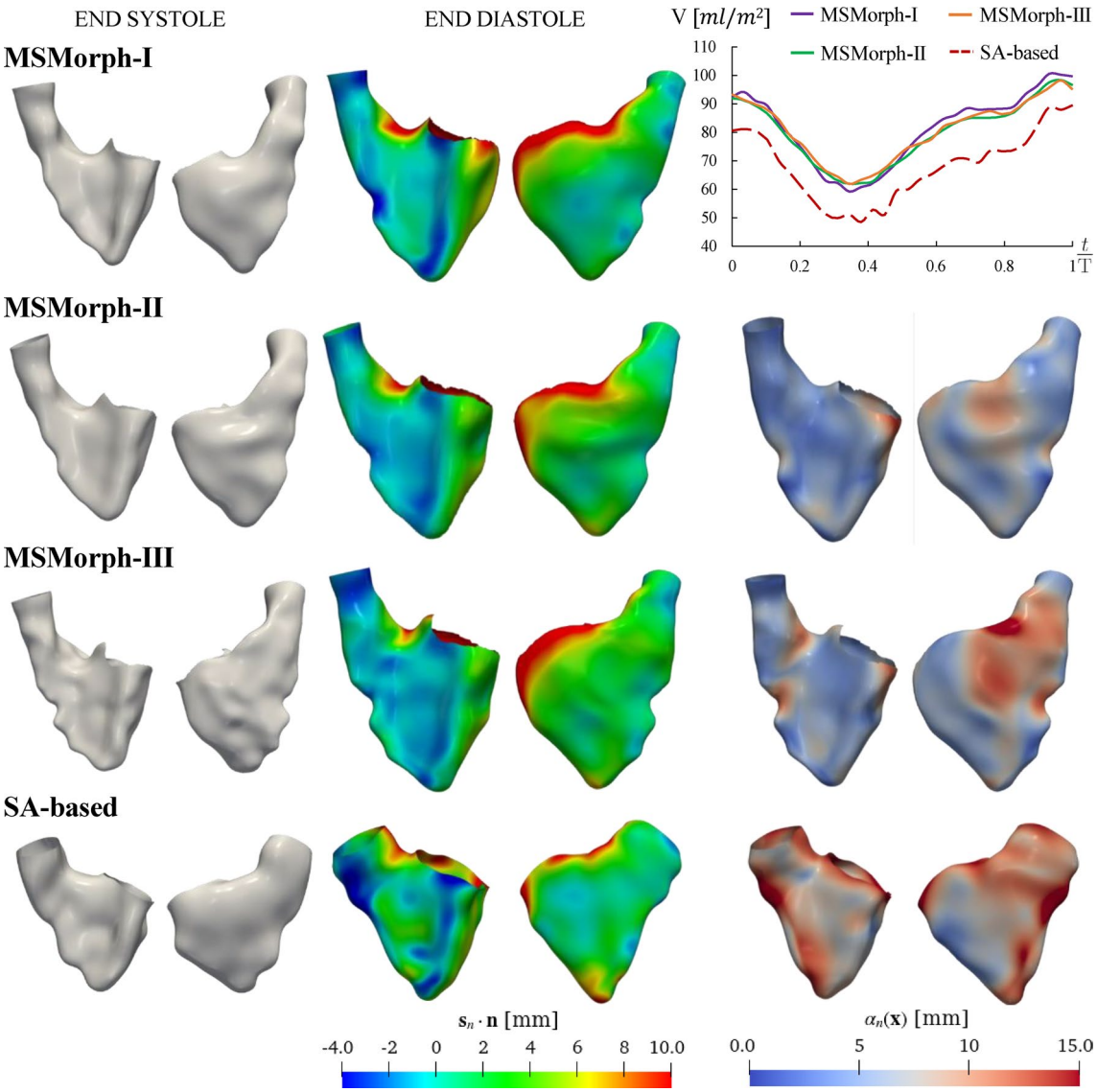

FIGURE 5 | RV reconstruction of a healthy patient. MSMorph-I: MSMorph technique employing all available cine-MRI; MSMorph-II: MSMorph technique employing all available cine-MRI apart TV-R cine-MRI; MSMorph-III: MSMorph technique employing only SA and LA cine-MRI; SA-based: standard reconstruction procedure [32] employing only SA cine-MRI. Left column: reconstruction of the reference end-systolic configuration. Central column: reconstruction of the end-diastolic configuration and spatial distribution of the normal component of the corresponding displacement field. Blue and light blue colors: inward normal displacement; Green, yellow, and red colors: outward normal displacement. Right column: on top, the time evolution of the ventricular volumes normalized w.r.t. body surface area, computed by removing the pulmonary artery; below, the spatial distribution of metric α_n defined on the end-diastolic configurations.

TABLE 1 | Values of $\text{TAMSD}(\tilde{\Gamma}_n, \tilde{\Lambda}_n)$ obtained for the healthy RV with different strategies.

MSMorph-I	MSMorph-II	MSMorph-III	SA-based
2.37 mm	2.81 mm	2.99 mm	4.42 mm

basal region of the ventricle and of the RVOT, which are areas not precisely acquired in SA cine-MRI. For these reasons, we will exclusively focus on the reconstructions obtained employing only the MSMorph procedures from now on.

Finally, in Table 2, we compare some volume indices obtained from our reconstructions with the reference ranges derived from cardiac MR for an adult male [42–44]. Although this comparison does not provide any validation of our results, it is important to demonstrate that our findings fall within standard reference ranges, underscoring their meaningfulness according to the authors' opinion. Considering these indices as normally distributed, we observe that in all scenarios the chamber volumes obtained by our method are larger than the average ones; however, they fall within three standard deviations from the mean values, encompassing 99.7% of the studied population. More specifically, in the case of MSMorph-I, they fall within two standard deviations (95.0% of the studied population). Moreover, the visual comparison between the reconstructed surfaces with the reference solution $\tilde{\Gamma}_n$ in Figure 7d,e appears to exclude the possibility of an overestimation of the chamber volumes for this subject. Indeed, we can observe that the reference contours lie mostly outside the reconstructed surfaces. Examining the

TABLE 2 | Volumetric indexes of the two cardiac chambers: The values obtained for MSMorph-I, MSMorph-II, MSMorph-III reconstructions are compared with reference ranges from cardiac magnetic resonance [42, 43].

				Reference ranges	
Index	**MSMorph-I**	**MSMorph-II**	**MSMorph-III**	**MEAN ± SD**	**[LL, UL]**
RA V_{max} $[mL/m^2]$	61.0	58.4	59.9	52 ± 12	[28, 76]
RA V_{preAC} $[mL/m^2]$	48.0	48.8	48.2	40 ± 10	[20, 60]
RA V_{min} $[mL/m^2]$	37.2	41.1	39.1	27 ± 9	[9, 45]
RV V_{max} $[mL/m^2]$	100.6	98.3	98.2	88 ± 17	[54,122]
RV V_{min} $[mL/m^2]$	59.2	61.9	61.9	38 ± 11	[16, 60]
RV SV $[mL/m^2]$	41.4	36.5	36.3	52 ± 12	[28, 76]
RV EF [%]	41.2	37.1	37.0	57 ± 8	[41, 73]

Abbreviations: AC, atrial contraction; LL, MEAN—2SD, lower limit; SD, standard deviation; UL, MEAN + 2SD, upper limit.

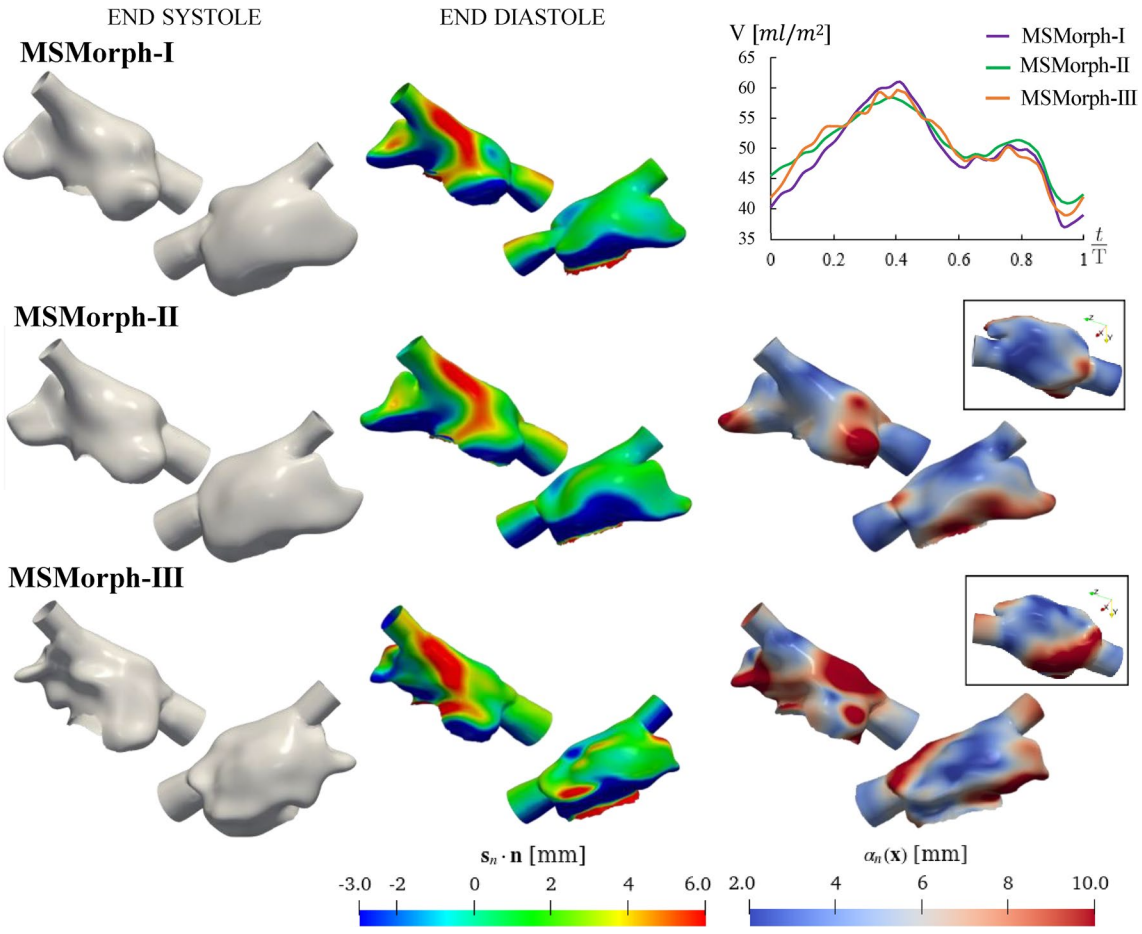

FIGURE 6 | RA reconstruction of a healthy patient. MSMorph-I: MSMorph technique employing all available cine-MRI; MSMorph-II: MSMorph technique employing all available cine-MRI apart TV-R cine-MRI; MSMorph-III: MSMorph technique employing only SA and LA cine-MRI. Left column: reconstruction of the reference end-systolic configuration. Central column: reconstruction of the end-diastolic configuration and spatial distribution of the normal component of the corresponding displacement field. Blue and light blue colors: inward normal displacement; Green, yellow, and red colors: outward normal displacement. Right column: on top, the time evolution of the atrial volumes normalized w.r.t. body surface area; below, the spatial distribution of metric α_n defined on the end-diastolic configurations.

ejection fraction (EF) values, it appears that MSMorph-II and MSMorph-III tend to underestimate the patient's EF. This underestimation can be attributable to an average lower accuracy characterizing these variants for which a reduced amount of information drives the morphing process. Thus, for patients with borderline EF, as in our case, these variants could lead to

estimates that should not be considered. However, for normal values of EF, this underestimation should lead to physiological EF ranges.

3.2 | Comparison of RA Reconstructions

In this section, we focus on the performance of the MSMorph procedure for the reconstruction of the RA of the H subject.

In Figure 6, we present the end-systolic MSMorph reconstructions in the left column and the end-diastolic MSMorph reconstructions along with the normal component of the end-diastolic displacement s_n in the central column. The right column of the same figure illustrates the distribution of parameter α_n over the end-diastolic reconstructions. As for the ventricle, MSMorph-I exhibits the smoothest and most detailed surface, where the auricle and the SVC are quite well-defined. Notably, the three MSMorph reconstructions diverge in the auricle and the coronary sinus, as shown by the distribution of α_n. The central column of Figure 6 shows that MSMorph-I and MSMorph-II share similar patterns of the normal displacement, while the normal displacement of MSMorph-III reconstruction differs mainly at the level of the auricle. In the top right plot, we report the evolution of RA volume over the heartbeat. The volume trend is consistent across the three MSMorph procedures. MSMorph-III RA reaches almost the same maximum and minimum volumes as MSMorph-I, while MSMorph-II differs by approximately 10% in the minimum volume and in the volumes at the beginning and end of the cycle compared with the MSMorph-I reconstruction.

Analyzing the discrepancy w.r.t. the reference solution, we find $\mathrm{TAMSD}(\tilde{\Gamma}_n, \tilde{\Lambda}_n)$ values of 3.4, 3.6, and 4.1 mm for MSMorph-I, MSMorph-II, and MSMorph-III respectively. These results suggest that the atrium MSMorph-I procedure performs better among the three techniques in atrial reconstruction.

Comparison with volume indices reported in the literature yields similar considerations for the atrium as were observed for the ventricle. Specifically, $V_{\max}$, V_{preAC}, and $V_{\min}$ fall at least within 2 standard deviations from the mean values found in the literature; see Table 2 [42–44].

TABLE 3 | Metrics for the analysis of the MSMorph procedure, computed for the RA and RV.

	$\mathrm{TAMSD}(\tilde{\Gamma}_n, \Gamma_n)$	$\mathrm{TAMSD}(\tilde{\Gamma}_n, \Lambda_n^{\mathrm{endo}})$	$\mathrm{TAMSD}(\Lambda_n^{\mathrm{endo}}, \tilde{\Lambda}_n)$
RA	1.47 mm	2.28 mm	0.65 mm
RV	2.34 mm	2.12 mm	0.53 mm

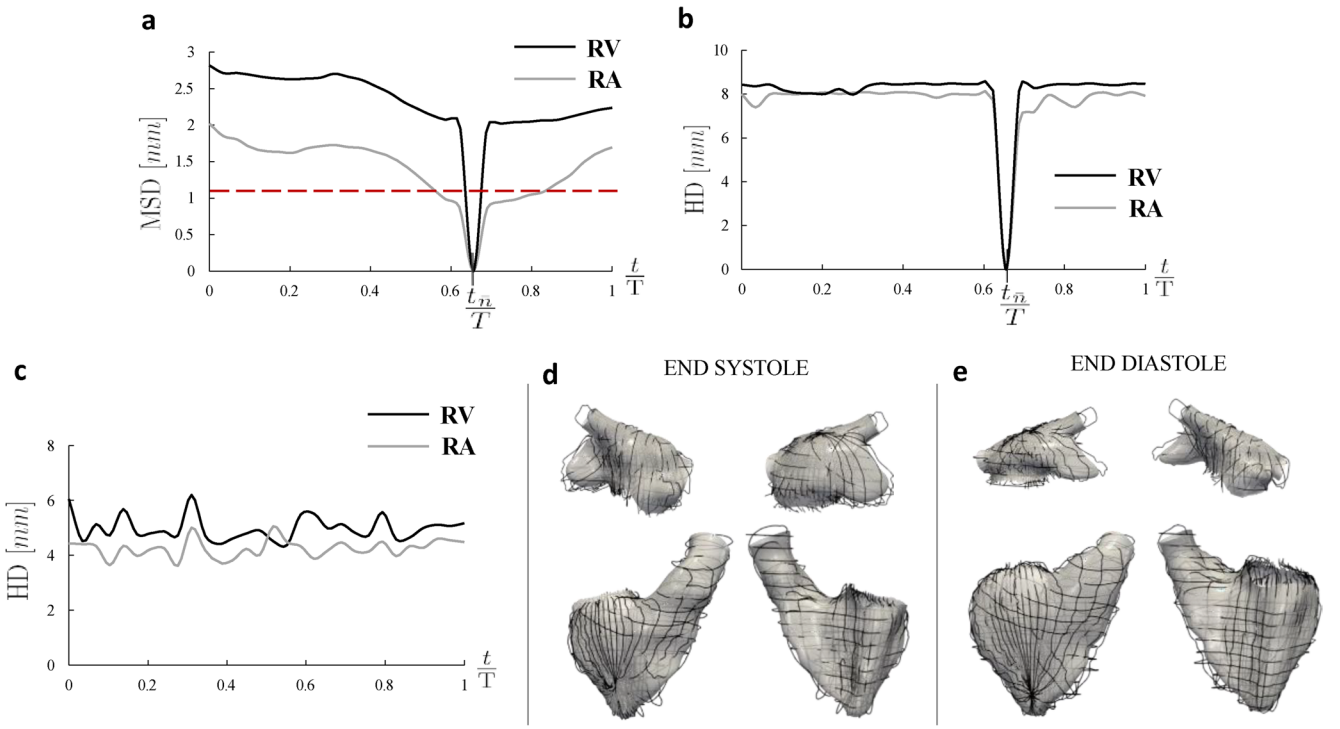

FIGURE 7 | (a, b): Evolution over time of MSD (left) and $\mathrm{HD}(\tilde{\Gamma}_n, \Gamma_n)$ (right) for the RA and the RV contours of the healthy subject. The red dotted line indicates the value of the in-slice resolution, 1.15 mm; (c): evolution over time of $\mathrm{HD}(\tilde{\Gamma}_n, \tilde{\Lambda}_n)$ for the RA and the RV of the healthy subject; Reconstructions of the RA and RV of the healthy subject (in grey) obtained at end systole (d) and at end diastole (e) compared with the reference solution $\tilde{\Gamma}_n$ (in black). MSMorph-I scenario.

3.3 | Analysis of MSMorph Steps

We investigate how the three main steps of the MSMorph procedure (see Section 2.2) introduce discrepancies w.r.t. the reference solution $\tilde{\Gamma}_n$, affecting the final reconstruction. The evaluation is performed using the metrics detailed in Section 2.4. For such analysis, we specifically focus on MSMorph-I, and the results are reported in Table 3 and Figure 7.

Concerning the *contour generation* step (Section 2.2.1), we set the initialization instant $t_{\bar{n}}$ of the registration algorithm the onset of diastasis, typically occurring around 60 % of the imaged heartbeat. As expected, Figure 7 shows that the MSD metric features a zero value at $t_{\bar{n}}$ and grows both for decreasing and increasing times due to the accumulation of errors along the propagation. This error distribution over time is not periodic (values of MSD_n at $t_{\bar{n}}/T = 0$ and $t_{\bar{n}}/T = 1$ are slightly different) consistently with the fact that the cardiac motion is inherently not symmetric. Maximum values of MSD are less than two and three times the in-plane slice resolution (1.15×1.15) mm for RA and RV, respectively. In particular, RV exhibits higher MSD than RA due to the prevalence of trabeculations, which challenges the contouring algorithm in endocardium recognition. Looking at the evolution over time of HD_n, reported in Figure 7, slightly higher HD values are still shown for RV, while the overall distribution is almost constant over time and approximately around 8 mm for both chambers.

Evaluating the discrepancies between the endocardial surface generated in Step 2 (*surface generation*, Section 2.2.2) and the reference solution using the metric $\mathrm{TAMSD}\left(\tilde{\Gamma}_n, \Lambda_n^{\mathrm{endo}}\right)$ (refer to Table 3), we find that the morphing procedure has a modest impact on the reconstruction accuracy, with this metric remaining under twice the in-plane slice resolution. Moreover, comparing the values of $\mathrm{TAMSD}\left(\tilde{\Gamma}_n, \Lambda_n^{\mathrm{endo}}\right)$ and $\mathrm{TAMSD}\left(\tilde{\Gamma}_n, \Gamma_n\right)$, reveals, in the case of RV, that the resulting surface is, on average, closer to the reference solution than the set of contours from which it is generated.

Regarding Step 3 (Section 2.2.3), we observe that the introduced discrepancies are negligible compared with the resolution of the involved images (Section 2.1).

Finally, in Figure 7c, we analyze the discrepancies between the reconstructed surfaces $\tilde{\Lambda}_n$, final output of the MSMorph procedure, and the reference solution $\tilde{\Gamma}_n$. We can observe that HD assumes lower values as compared with $\mathrm{HD}\left(\tilde{\Lambda}_n, \Gamma_n\right)$ (Figure 7b) for both RA and RV chambers. This seems to suggest that the steps following the generation of the contours may help reduce the maximum discrepancy between the reconstructed surfaces and the reference solution. However, further investigations are mandatory to confirm this speculation.

3.4 | Reconstruction of a RH With Repaired ToF

For the patient with repaired Tetralogy of Fallot (TF), cine-MRI acquisitions include SA, LA, 2, 3, and 4 Ch views. However, due to the absence of ad-hoc acquisitions for the RA, accurate reconstruction of its auricle is challenging, as evident in Figure 8, where TF's RH reconstruction is compared with that of the H individual.

The reconstructed RV surface is qualitatively in accordance with the cine-MRI, as illustrated in Figure 8 by the yellow line representing the intersection between the image plane and the reconstructed surface. Indexed RV and RA EDV are 184.4 and 48.79 mL/m^2, respectively, falling within the ranges for repaired ToF found in the literature [45]. From the analysis of the volume and flow rate curves (Figure 8), reduced contractile activity of RA in determining the diastolic RV filling is observed compared with the healthy case, and the final end-diastolic volume is almost reached at the onset of diastasis. This indicates a reduced reservoir function and increased conduit function, which are typical characteristics of repaired ToF patients [45–47].

Remark 2. Notice that in the case of this patient, dedicated TV-R cine-MRI acquisitions for the RA reconstruction were unavailable. Instead, we relied on SA, LA, and 2/3/4 Ch views where the atrium was visible. It is important to highlight that, while not addressed in this study, other cine-MRI views have been used. For instance, in the work of [48] the left atrium was reconstructed using LA and rotational-mitral valve (MV-R) cine-MRI.

3.5 | Discussion

Given the critical relationship between cardiac blood dynamics and heart function, being able to correctly and accurately reconstruct the RH and its motion is of utmost importance in view of computational blood dynamics analysis. In this study, we presented a new method (MSMorph) capable of accurately reconstructing the RH geometry together with its motion by processing multi-series images, including Short-Axis (SA), Long-Axis (LA), 2/3/4-chambers (2/3/4-Ch), and rotational cine-MRI (TV-R), in a unique fashion. Thanks to this leveraging of multiple views, our method can provide through-plane motion information, although not originally available in the cine-MRI.

We applied our method to reconstruct the right ventricle (RV) and pulmonary artery (PA) of a healthy subject (H), and we quantified the accuracy in this control case. To evaluate the influence of different types and numbers of cine-MRI series on the reconstruction process, we presented three different MSMorph variants obtained using different cine-MRI acquisitions. In addition, we reconstructed the RV and PA of the same healthy subject using a procedure based solely on SA images, to compare the performance of such variants with standard techniques introduced so far in the literature. In the absence of an appropriate ground truth geometry and motion reconstructions, we considered the endocardial contours manually traced on the images under the supervision of clinical experts as a reference solution to validate our results on the real data. Our results demonstrated that MSMorph outperforms the standard reconstruction procedure in terms of fidelity to the images. Moreover, we proved that the proposed method is able to successfully handle complex morphologies, such as the right atrium (RA) of H and the RH of a repaired Tetralogy of Fallot patient (TF).

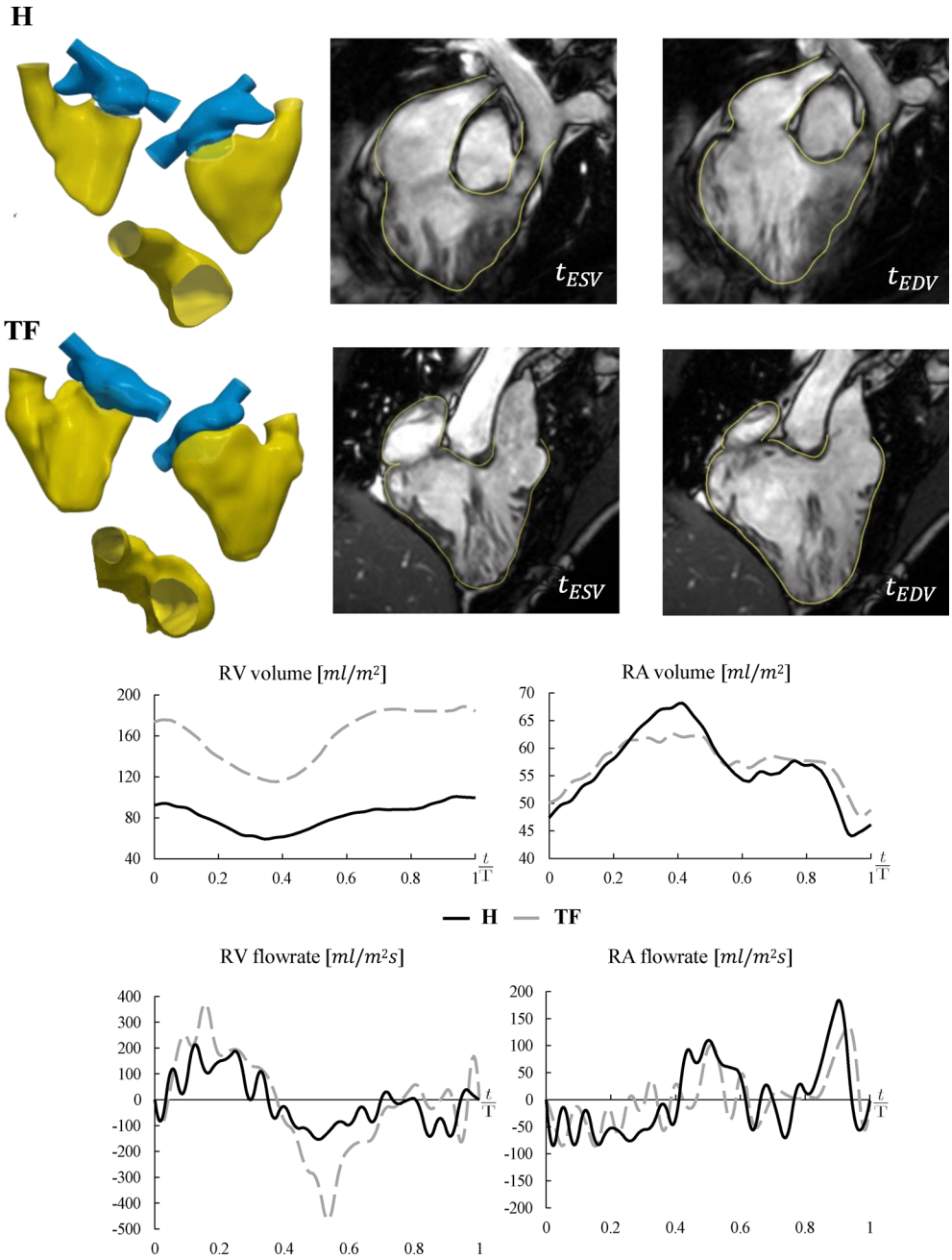

FIGURE 8 | RH reconstruction of a healthy subject (H) and a ToF patient (TF). First–second rows: RH reconstructions and intersections of the reconstructed surfaces with the image plane at two instants of the cardiac cycle; first row: healthy subject; second row: ToF patient. Third row: RV and RA volume curves over a heartbeat. Fourth row: curves of RV and RA flow rates over a heartbeat computed as the time derivative of the volumes multiplied by the blood density.

These results also provided a new solution to face challenging issues associated with the RH reconstruction over the entire heartbeat, such as the management of its complex morphology and motion. Indeed, unlike the left ventricle, which has a prolate ellipsoid shape, the RV is characterized by a more irregular geometry with a cone-shaped outflow tract that protrudes outside the chamber. The RA also has anatomically complex regions, such as the auricle and the coronary sinus. This morphological complexity, together with the fact that the RH movement occurs mostly along the longitudinal direction, makes the RH reconstruction very challenging when only SA cine-MRI series are considered since the atrioventricular plane changes its slice location during the cardiac cycle. Thus, the inclusion of images taken along different planes, such as TV-R, 2/3/4 Ch, and LA cine-MRI, is essential to overcome these hurdles in the reconstruction procedure. In this respect, the MSMorph procedure is a valuable and efficient tool to merge the differently oriented cine-MRI views without requiring additional image processing for resolution enhancement in the through-slice direction [13, 26]. This was able owing to our new idea of morphing a surface over the set of contours semi-automatically traced directly on the original available cine-MRI, where the endocardium is clearly identifiable.

This merging of different cine-MRI especially allows the accurate reconstruction of the RH at the atrioventricular plane, an

area usually cut off in the reconstructions obtained only with SA cine-MRI. We believe that this accurate reconstruction is a relevant contribution of our study since it facilitates the correct quantification of the cardiac chamber volumes and contractility, with crucial implications in the clinical practice. Moreover, this makes possible the correct insertion of the valves in the computational model and, therefore, leads to realistic modeling of blood-valve interaction.

Another notable feature of MSMorph relies on its ability to reconstruct the whole heartbeat RH geometry and motion starting from the manual contouring of the endocardium for just one frame., thanks to the semi-automatic 2D-registration algorithm detailed in Section 2.2.1. The low error accumulation compared with the mean resolution of the images, which is about 3 mm (see Figure 7 and Table 1) and the ability to provide (potentially) a family of reconstructions depending on the richness and diversity of the available cine-MRI series and plane orientations (see variants MSMorph-I, MSMorph-II, and MSMorph-III, and Section 2.4) further emphasize the versatility and robustness of the MSMorph technique. Indeed, this allowed us to capture more geometric details when considering richer datasets, such as the coronary and pulmonary sinuses (Figures 5 and 6). On the contrary, we found an increasing presence of surface artifacts when considering less rich datasets due to the progressive absence of constraints coming from the missing TV-R and AV-SA contours, which play the role of driving the template deformation during morphing. In particular, RA seemed to be more sensible to the richness of the datasets w.r.t. the RV due to its more complex morphology (refer to Figure 6 and Section 3.2).

Despite local differences experienced by the dataset variants, MSMorph showed to obtain robust results about global quantities (see, e.g., the volumes in Figures 5 and 6). The method shows mild variations (about $3\% - 4\%$) in RA and RV volumes over the heartbeat among the three techniques, highlighting its flexibility w.r.t. the input data being able to produce reasonably good results also when few images are available, provided that SA and LA cine-MRI are suitably enriched.

Although in this study we have provided two instances of potential adaptations of the MSMorph technique to the number and type of available cine-MRI views (MSMorph-II, MSMorph-III), our technique allows for various other permutations, as mentioned in Remark 2. For instance, one could consider using the complete TV-R and SA stacks while discarding the LA cine-MRI.

Moreover, the method proves to be very flexible w.r.t. the morphology of the object to reconstruct. In particular, MSMorph was successfully applied to RH chambers and valves as well (Figure 4); see also [48] for an application to the left ventricle and atrium. MSMorph proves to be versatile also w.r.t. the possible presence of geometric defects leading to malfunctioning, such as in repaired ToF (Figure 8).

Potential clinical applications of the methods described herein exist. One practical field of investigation relates to the definition of indications and timing of pulmonary valve replacement in repaired ToF. Whereas MRI indices of RH dysfunction, useful for surgical indications, have already been proposed, these are still debated due to limitations in estimating RH dysfunction and predicting its recovery [49, 50]. Translational research has also been applied to this clinical scenario in an attempt to further understand the pathophysiology of RH changes after surgical pulmonary valve replacement [51]. The current method has the potential to add evidence supporting the benefits of interventions aimed at improving RH function.

We notice that MSMorph does not require any training procedure, based on the collection of a big dataset, as needed by machine learning-based techniques [28, 30, 31, 52].

4 | ID-CID Model

For the modeling of blood flow, we consider the Navier–Stokes equations in a moving domain under the assumption that blood behaves as an incompressible Newtonian fluid in large vessels and heart chambers [53]. The displacement of the RH domain $\Omega(t)$, reconstructed from images as described in Section 2.2.3, is prescribed as boundary motion for the fluid domain problem consisting in a linear elasticity extension [54], and it is used to compute the wall velocity for the fluid problem solved in an Arbitrary Lagrangian–Eulerian (ALE) formulation [55, 56]. Specifically, the motion of $\Omega(t)$ is determined at time instants $t_n, n = 0, \dots, N$, by the reconstructed displacement field $\boldsymbol{s}_n(\hat{\boldsymbol{x}})$, referred to the reference configuration. To recover the displacement field (and thus the computational domain) for each time instant, we used a spline interpolation to obtain $\boldsymbol{s}(\hat{\boldsymbol{x}}, t)$ for all $t \in [0, T]$.

The valves are modeled as surfaces immersed in the fluid dynamics domain managed by the resistive immersed implicit surface (RIIS) method [7, 57, 58], accounting for the opening/closure of the two valves by means of an on–off modality and selecting a priori the opening/closure instants by the images [32].

Finally, to account for turbulence transition that may develop, we consider the Large Eddy Simulation σ-model [59], which has already been extensively used in many hemodynamics applications [60–62].

In this framework, referring to Figure 3a, the continuous problem reads:

$$\begin{cases} \rho\left[\dfrac{\delta \boldsymbol{u}}{\delta t} + \left(\left(\boldsymbol{u} - \boldsymbol{u}_{\mathrm{ALE}}\right)\cdot\nabla\right)\boldsymbol{u}\right] - \nabla\cdot\boldsymbol{\sigma}(\boldsymbol{u}, p) + \mathscr{R}(\boldsymbol{u}) = \boldsymbol{0} & \text{in } \Omega(t), \\ \nabla\cdot\boldsymbol{u} = 0 & \text{in } \Omega(t), \\ \boldsymbol{\sigma}(\boldsymbol{u}, p)\cdot\boldsymbol{n} = -p_{\mathrm{in}}\boldsymbol{n} & \text{on } \Sigma_{\mathrm{in}}(t), \\ \boldsymbol{\sigma}(\boldsymbol{u}, p)\cdot\boldsymbol{n} = -p_{\mathrm{out}}\boldsymbol{n} & \text{on } \Sigma_{\mathrm{out}}(t), \\ \boldsymbol{u} = \dfrac{\partial \boldsymbol{s}}{\partial t} & \text{on } \Sigma_{\mathrm{w}}(t), \end{cases} \tag{8}$$

where $\boldsymbol{u}$ and p are the blood velocity and pressure, respectively, $\frac{\delta}{\delta t}$ is the time-derivative in the ALE-framework, ρ denotes the blood density and $\boldsymbol{\sigma}$ the stress tensor defined as:

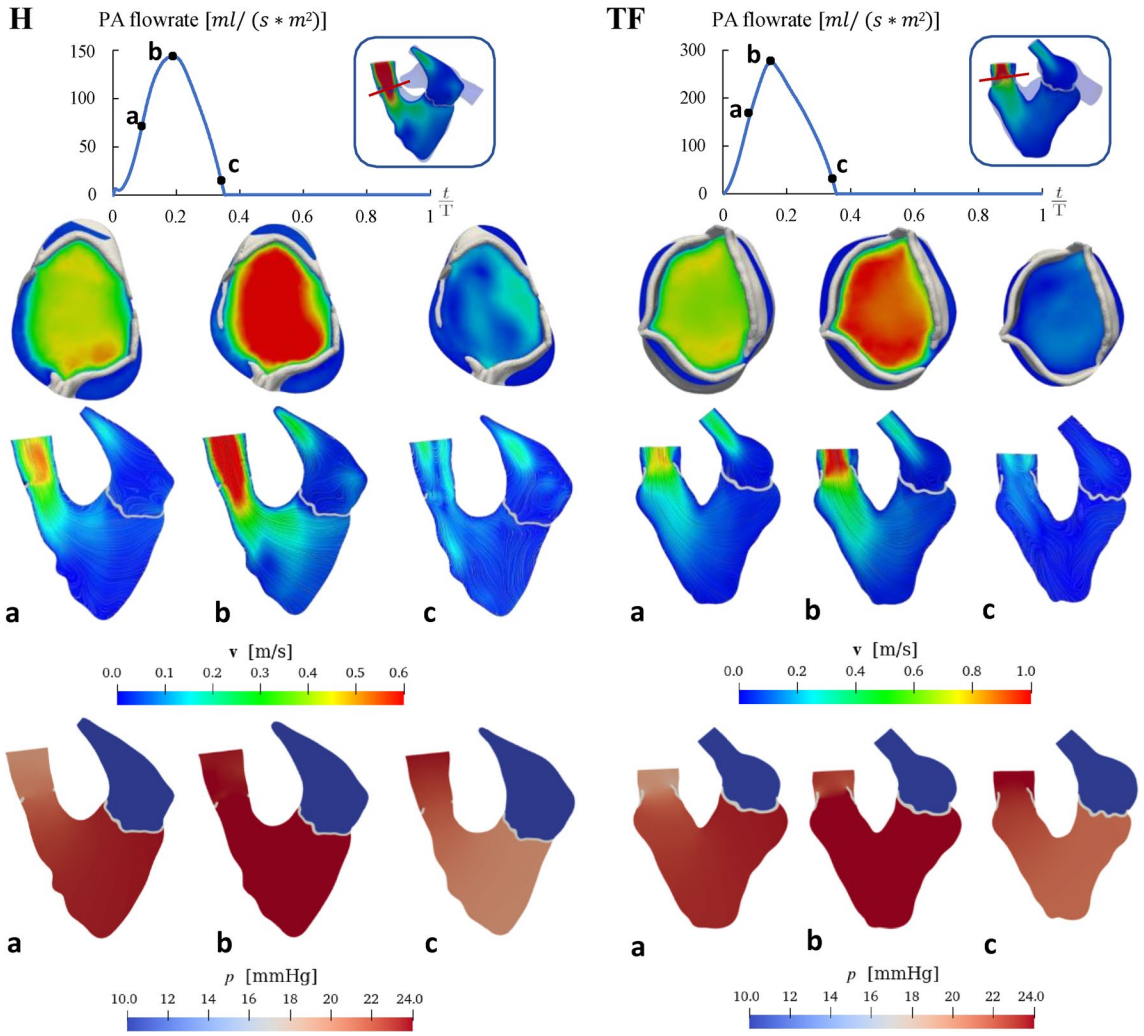

FIGURE 9 | First row: selected time instants and longitudinal and transversal (in red) sections where velocity is plotted; second row: velocity field on the longitudinal section: Third row: velocity field on the transversal section; fourth row: pressure field on the longitudinal section. Left: healthy subject (H); right: patient with repaired ToF (TF). (a): acceleration phase; (b) systolic peak; (c): deceleration phase.

$$\boldsymbol{\sigma}(\boldsymbol{u},p)=\left(\mu+\mu_{\text{sgs}}\right)\left(\nabla\boldsymbol{u}+\nabla\boldsymbol{u}^{T}\right)-p\boldsymbol{I} \tag{9}$$

with μ the blood dynamic viscosity. The parameter μ_{sgs} is the sub-grid viscosity of the σ-model [59], defined as $\mu_{\text{sgs}}=\rho C\Delta^2\sigma_3(\sigma_1-\sigma_2)(\sigma_2-\sigma_3)/\sigma_1^2$. Here, σ_1, σ_2, and σ_3 are the singular values of $\nabla\boldsymbol{u}$ and Δ is the average mesh size. Moreover, $p_{\text{in}}(t)$ and $p_{\text{out}}(t)$ are two given functions of time representing suitable pressure curves. We have also $\mathscr{R}(\boldsymbol{u})=\sum_{i=\text{TV,PV}}\frac{R_i}{\epsilon_i}(\boldsymbol{u}-\boldsymbol{u}_{\Gamma_i})\delta_{\Gamma_i,\epsilon_i}$ is a resistive term which allows to account for the presence of the valves, where R_i and ϵ_i are user-defined positive coefficients, and u_{Γ_i} is the prescribed leaflet velocity. In this study, we set $\boldsymbol{u}_{\Gamma_i}=\boldsymbol{0}$, $i=\text{TV, PV}$, since we are not modeling the opening and closure dynamics. We refer to [63] for a detailed description of the RIIS method and the parameters it involves. Finally, in the above system, $\boldsymbol{u}_{\text{ALE}}$ is the fluid domain velocity defined as the time derivative of the fluid domain displacement $\widehat{\boldsymbol{d}}$. The latter is obtained as the solution to the following lifting problem solved in the reference configuration $\widehat{\Omega}$:

$$\begin{cases}-\nabla\cdot\left(c\alpha\widehat{\boldsymbol{T}}\left(\widehat{\boldsymbol{d}}\right)\right)=\boldsymbol{0} & \text{in } \widehat{\Omega},\\ \widehat{\boldsymbol{d}}(\boldsymbol{x},t)=\widehat{\boldsymbol{s}}(\boldsymbol{x},t) & \text{on } \widehat{\Sigma}_{\text{w}},\\ \widehat{\boldsymbol{T}}\left(\widehat{\boldsymbol{d}}\right)\widehat{\boldsymbol{n}}=\boldsymbol{0} & \text{on } \widehat{\Sigma}_{\text{in}}\cup\widehat{\Sigma}_{\text{out}},\end{cases} \tag{10}$$

where T is the linear elasticity Hooke tensor characterized by the Lame' constants λ and ν, $c(\widehat{\boldsymbol{x}})$ and $\alpha(\widehat{\boldsymbol{x}})$ are functions which penalise excessive distortion of the computational mesh elements during the simulation [63]. Specifically, $\alpha(\widehat{\boldsymbol{x}})=\max(d(\widehat{\boldsymbol{x}}),\beta)^{-\gamma}$, where $d(\widehat{\boldsymbol{x}})$ is the distance from the boundary $\partial\Omega$ [64] and the parameters β and γ are tuned to increase the stiffness of the mesh in the elements that are closer to the boundary; $c(\widehat{\boldsymbol{x}})=\left(\frac{J_0}{J(\widehat{\boldsymbol{x}})}\right)^{\chi}$, where J_0 and χ are positive user-defined parameters, and $J(\widehat{\boldsymbol{x}})$ is the Jacobian of the map from the unit reference element to $\widehat{\Omega}$ [54] and aims at increasing the stiffness of the smaller elements.

Once we have solved problem (10), we can recover the current computational domain at time t as follows:

$$\Omega(t) = \left\{ \boldsymbol{x} \in \mathbb{R}^3 : \boldsymbol{x} = \hat{\boldsymbol{x}} + \hat{\boldsymbol{d}}(\hat{\boldsymbol{x}}, t), \hat{\boldsymbol{x}} \in \hat{\Omega} \right\}.$$

5 | ID-CFD Analysis: Results and Discussion

The fluid-dynamics problem in the moving domain described in Section 4 is solved for the healthy (H) and the pathological (TF) cases by the Finite Elements library `life`^{x} [63, 65] (developed at MOX, Politecnico di Milano, within the framework of the iHEART project https://iheart.polimi.it/).

The tetrahedral meshes of H and TF RHs together with their valves are generated using suitable vmtk algorithms with average mesh size of 2 mm. A local refinement of 0.2 mm has been performed close to the PV and TV (see Figure 4b,c).

For the time discretization of the ID-CFD problem, we employ a semi-implicit backward Euler scheme with time-step $\Delta t = 10^{-4}\,s$. In space, we adopt first-order Finite Elements with PSPG-SUPG stabilization [66]. For the fluid problem we set $R = 1e4,\ \epsilon = 4e-4, \rho = 1.06\ \mathrm{kg/m^3}, \mu = 0.0035$ Pa m. Physiological pressures prescribed at the SVC and IVC inlets Σ_{in} and at the PA outlet Σ_{out} are taken from 41 and depicted in Figure 4d. Concerning the parameters for the lifting problem Equation (10), we set $\beta = 0.09$ mm, $\gamma = 0,05, J_0 = 5e-9, \chi = 1.0$, $\lambda = 0.84$ Pa, and $\nu = 0.44$ Pa.

In Figure 9, we report the velocity and pressure fields for the considered subjects at three instants during systole. The maximum in the velocity field is reached at the systolic peak at the level of the PV orifice, and it is 1.13 and 0.9 m/s for TF and H, respectively. H is characterized by a mean pressure drop during systole of 0.5 mmHg across the open TV and of 15.5 mmHg across the closed TV, while TF valves are characterized by 2.0 and 16.5 mmHg, respectively. Figure 10 reports the sub-grid viscosity μ_{sgs} for the two subjects at the above-specified instants, together with vortical structures identified by the Q-criterion > 3000. In particular, we can observe the development of vortical structures downwind PV and near the ventricular-facing side of the PV's leaflets, which are almost dissipated at end-systole. These regions experience a transition to turbulence, as shown by elevated values of sub-grid viscosity; in particular, μ_{sgs} reaches values at least five times greater than the value of physical viscosity.

These results showed that the MSMorph outcomes provide suitable time-resolved 3D geometric data for image-driven CFD of the RH, facilitating the quantification of relevant quantities such as blood pressures and turbulence. Since MSMorph is almost completely automatic, it allowed us to obtain the input data for ID-CFD in a few hours, dramatically shortening the time commonly needed to reconstruct the whole heartbeat of the RH. For example, with the SA-based procedure, the preprocessing of the healthy subject H required about 55 h. This accelerates the workflow from medical image acquisition to blood-dynamics analyses and could be of particular relevance for clinical applications such as the study of the performance of PV replacement or tricuspid regurgitation. Moreover, the resulting RH displacement field was smooth enough to minimize the occurrence of mesh distortion, which is one of the major causes of failure during ID-CFD simulations. Regarding the numerical results, we were able to assess the primary quantities velocity and pressure, as well as relevant post-processed quantities, for example, turbulence. Notice that the computed fluid-dynamic quantities (Figures 9 and 10) were reasonable and in agreement with expectations.

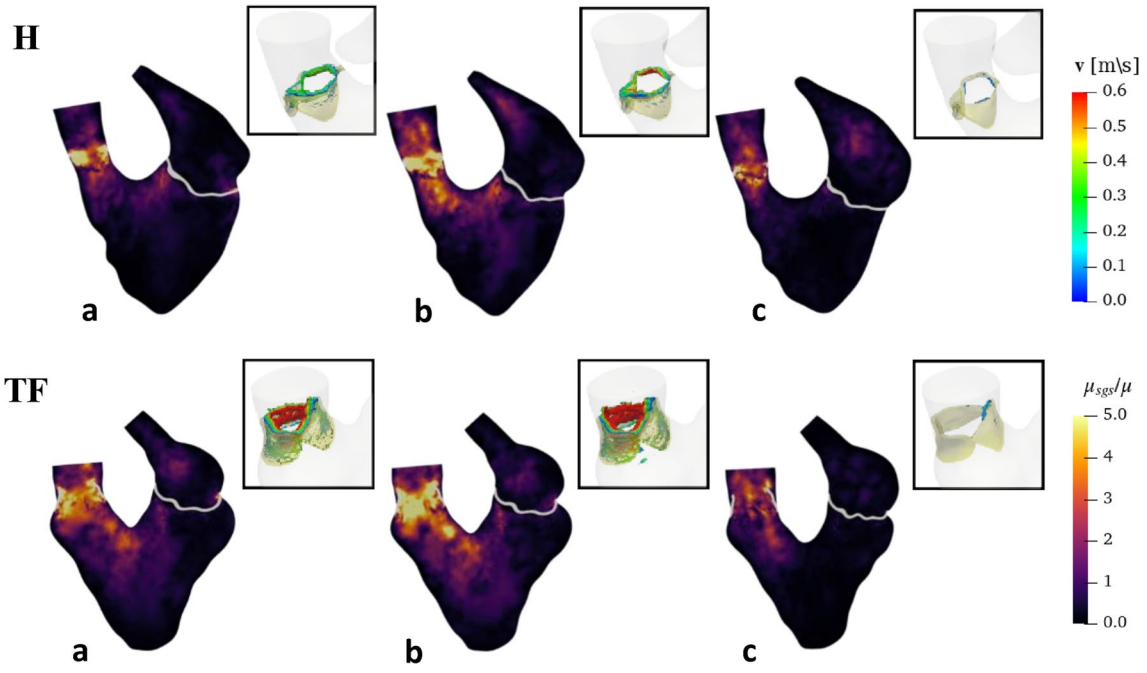

FIGURE 10 | Sub-grid viscosity μ_{sgs} normalized w.r.t. the blood viscosity μ on the longitudinal section for H (first row) and TF (second row) at the three selected instants. Windows to focus on vorticity isosurfaces at RVOT created with Q criterion > 3000.

In particular, for the healthy case, the peak velocity at the PV orifice fell in the physiological range $0.8 - 1.2$ m/s [67, 68], whereas the RA and RV pressures fell in the physiological ranges $15 - 30$ and $0 - 8$ mmHg, respectively [69]. For the TF case, although we did not prescribe a proper outlet pressure condition, we could appreciate an increase in the blood velocity at peak systole, in the RA and RV pressures, in the TV and PV pressures, and in the vorticity values, w.r.t. H case.

In the authors' opinion, the easy usability in view of ID-CFD is another important contribution of MSMorph to the comprehension of RH.

6 | Limitations and Future Developments

This study is characterized by some limitations discussed in what follows.

- Some of the cine-MRI datasets used in this study (especially the TV-R series) do not yet represent standard acquisitions performed in clinical practice. However, we believe that our study provides an important step toward using cine-MRI multi-series in view of future analyses when they will become routinely available. In any case, thanks to the MSMorph-III variant, we were able to find acceptable results by using only the standard SA and LA cine-MRI series;
- We analyzed only two patients. In view of a routine use of the MSMorph procedure, a larger cohort of both healthy subjects and patients with different RH pathologies will be necessary in future investigations. In any case, we believe that the results found in this work are very promising and could provide an excellent starting point for future studies;
- Before the application of the MSMorph method, no initial realignment of acquired cine-MRI series has been implemented to overcome the slice misalignment due to breath-hold-related issues and/or patient movements during the image acquisition [26];
- The movement of obliquely oriented trabeculations and other structures near the endocardial wall across the fixed imaging plane of the corresponding cine-MRI view can generate spurious motions. These movements could impact the quality of the registration between subsequent slices. To address this challenge, potential strategies could involve the inclusion of an additional term in the cost function minimized by the registration algorithm. This additional term would penalize excessive and non-time coherent deformations arising from the appearance of such structures within the slice plane;
- The proposed reconstruction method is not actually able to manage trabeculae due to the inadequate spatial resolution of the available images;
- We used HD, MSD, TAMSD, and α_n as metrics to evaluate the accuracy of the proposed reconstruction method and the quality of the reconstruction results. For future studies, the computation of Intersection over Union and Dice coefficient parameters could be introduced to improve the understanding of the percentage of ground truth volume captured by the method. However, in this study, we did not have at our disposal ground truth segmented masks that would be needed for such computation.
- We performed a "2D validation" obtained against contours reconstructed manually. In view of the utility of the proposed method, a "3D validation" should be performed. This would require acquisitions characterized by a high resolution along the acquisition direction, as happens for example for CT images. However, we do not have at disposal such series from the diagnostic exam, and we cannot request either dedicated CT or high-resolution acquisitions as they would be outside its scope.
- We prescribed the physiological pressure displayed in Figure 4 as an outlet boundary condition at the pulmonary artery for the TF case. This is not properly correct since pressure for TFs is expected to be slightly higher. However, due to the high variability of pressure for TFs and the absence of proper pressure measurements, we decided to use the same pressure curve for both the analyzed cases. The imposition of suitable pressure boundary conditions for ToF will be mandatory in future blood-dynamics studies;
- The ID-CFD results have been quantitatively analyzed only w.r.t. literature values. Comparison of blood-dynamics results obtained by using MSMorph outcomes as input data with patient-specific measurements, such as echo-Doppler measures, will be mandatory.

Besides the improvements suggested by the previous limitations, further improvements of this study are:

- The use of pre-processing techniques to improve image resolution (e.g., the merge of SA and LA cine-MRI series provided in [13]) could be used in the *contour generation* step (1b in Figure 2) together with a 3D-registration algorithm. This will allow to semi-automatically generate the contours in place of the 2D-registration algorithm proposed in this study, to improve the efficiency of the procedure;
- The introduction of a penalization term in the morphing procedure could be considered to prevent the occurrence of unrealistic surface irregularities due to a lack of information coming from the available images;
- In the morphing procedure, the use of the surface obtained at the previous time step as the starting template surface for the current time step, instead of the sphere template considered in this study, could be considered an alternative to help the algorithm to satisfy the stopping criterion in a smaller number of iterations, since it would start from an initial condition closer to the desired surface configuration.

Acknowledgments

Francesca Renzi and Christian Vergara are members of the INdAM group GNCS "Gruppo Nazionale per il Calcolo Scientifico" (National Group for Scientific Computing). Christian Vergara has been partially supported by the Italian Ministry of University and Research (MIUR) within the PRIN (Research projects of relevant national interest) "MIUR PRIN22-PNRR n. P20223KSS2" Machine learning for fluid–structure interaction in cardiovascular problems: efficient solutions, model

reduction, inverse problems, and by the Italian Ministry of Health within the PNC PROGETTO HUB—DIAGNOSTICA AVANZATA (HLS-DA) "INNOVA," PNC-E3-2022-23683266–CUP: D43C22004930001, within the "Piano Nazionale Complementare Ecosistema Innovativo della Salute"—Codice univoco investimento: PNC-E3-2022-23683266. The authors would like to thank the iHEART Team for the technical support on life^x.

Conflicts of Interest

The authors declare no conflicts of interest.

Data Availability Statement

Research data are not shared.

Endnotes

[1] With *volumetric series*, we mean a sequence of 2D acquisitions made in a specific direction, that is, short axis, rotated, ... In the literature, sometimes they are referred to as *3D series*. Thus, long-axis 2, 3, and 4 chambers cine-MRI do not provide, in general, a volumetric series since they are often acquired on a single slice. Notice that, in any case, we cannot obtain a 3D volume directly from imaging; a reconstruction procedure is always needed, even for high-resolution technologies like CT.

[2] In this study, we always use a sphere as a template surface.

[3] Notice that $\Theta_{n,(j-1)}$ is composed by the projection of the set Γ_n on $\Lambda_{n,(j-1)}$.

[4] From now on, we indicate the Lagrangian quantities refererred to the reference configuration with the $\frown$.

References

1. S. I. Dumitrescu, I. C. Ţintoiu, and M. J. Underwood, *Right Heart Pathology: From Mechanism to Management* (Cham: Springer, 2018).

2. M. Bucelli, A. Zingaro, P. C. Africa, I. Fumagalli, L. Dede', and A. Quarteroni, "A Mathematical Model That Integrates Cardiac Electrophysiology, Mechanics, and Fluid Dynamics: Application to the Human Left Heart," *International Journal for Numerical Methods in Biomedical Engineering* 39, no. 3 (2023): e3678.

3. V. Meschini, R. Mittal, and R. Verzicco, "Systolic Anterior Motion in Hypertrophic Cardiomyopathy: A Fluid–Structure Interaction Computational Model," *Theoretical and Computational Fluid Dynamics* 35, no. 3 (2021): 381–396.

4. D. Tang, C. Yang, T. Geva, and J. Pedro, "Image-Based Patient-Specific Ventricle Models With Fluid–Structure Interaction for Cardiac Function Assessment and Surgical Design Optimization," *Progress in Pediatric Cardiology* 30, no. 1–2 (2010): 51–62.

5. C. M. Augustin, A. Crozier, A. Neic, et al., "Patient-Specific Modeling of Left Ventricular Electromechanics as a Driver for Haemodynamic Analysis," *Europace* 18, no. suppl_4 (2016): iv121–iv129.

6. E. Karabelas, M. A. Gsell, C. M. Augustin, et al., "Towards a Computational Framework for Modeling the Impact of Aortic Coarctations Upon Left Ventricular Load," *Frontiers in Physiology* 9 (2018): 538.

7. A. This, L. Boilevin-Kayl, M. A. Fernández, and J. F. Gerbeau, "Augmented Resistive Immersed Surfaces Valve Model for the Simulation of Cardiac Hemodynamics With Isovolumetric Phases," *International Journal for Numerical Methods in Biomedical Engineering* 36, no. 3 (2020): e3223.

8. H. Watanabe, T. Hisada, S. Sugiura, I. J. Okada, and H. Fukunari, "Computer Simulation of Blood Flow, Left Ventricular Wall Motion and Their Interrelationship by Fluid-Structure Interaction Finite Element Method," *International Journal Series C Mechanical Systems, Machine Elements and Manufacturing* 45, no. 4 (2002): 1003–1012.

9. A. Zingaro, I. Fumagalli, L. Dede, et al., "A Geometric Multiscale Model for the Numerical Simulation of Blood Flow in the Human Left Heart," *Discrete and Continuous Dynamical Systems–S* 15 (2022): 2391–2427.

10. A. Zingaro, M. Bucelli, R. Piersanti, F. Regazzoni, L. Dede, and A. Quarteroni, "An electromechanics-driven fluid dynamics model for the simulation of the whole human heart," (2023), *arXiv preprint*, arXiv:2301.02148.

11. L. Bennati, C. Vergara, V. Giambruno, et al., "An Image-Based Computational Fluid Dynamics Study of Mitral Regurgitation in Presence of Prolapse," *Cardiovascular Engineering and Technology* 14 (2023): 1–19.

12. C. Chnafa, S. Mendez, and F. Nicoud, "Image-Based Simulations Show Important Flow Fluctuations in a Normal Left Ventricle: What Could Be the Implications?," *Annals of Biomedical Engineering* 44 (2016): 3346–3358.

13. I. Fumagalli, P. Vitullo, C. Vergara, et al., "Image-Based Computational Hemodynamics Analysis of Systolic Obstruction in Hypertrophic Cardiomyopathy," *Frontiers in Physiology* 12 (2022): 787082.

14. Y. H. Loke, F. Capuano, E. Balaras, and L. J. Olivieri, "Computational Modeling of Right Ventricular Motion and Intracardiac Flow in Repaired Tetralogy of Fallot," *Cardiovascular Engineering and Technology* 13, no. 1 (2022): 41–54.

15. J. Mangual, F. Domenichini, and G. Pedrizzetti, "Describing the Highly Three Dimensional Right Ventricle Flow," *Annals of Biomedical Engineering* 40, no. 8 (2012): 1790–1801.

16. A. This, H. G. Morales, O. Bonnefous, M. A. Fernández, and J. F. Gerbeau, "A Pipeline for Image Based Intracardiac CFD Modeling and Application to the Evaluation of the PISA Method," *Computer Methods in Applied Mechanics and Engineering* 358 (2020): 112627.

17. H. Wiputra, C. Q. Lai, G. L. Lim, et al., "Fluid Mechanics of Human Fetal Right Ventricles From Image-Based Computational Fluid Dynamics Using 4D Clinical Ultrasound Scans," *American Journal of Physiology–Heart and Circulatory Physiology* 311, no. 6 (2016): H1498–H1508.

18. D. Collia, L. Zovatto, G. Tonti, and G. Pedrizzetti, "Comparative Analysis of Right Ventricle Fluid Dynamics," *Frontiers in Bioengineering and Biotechnology* 9 (2021): 667408.

19. A. Ammari, R. Mahmoudi, B. Hmida, R. Saouli, and M. H. Bedoui, "A Review of Approaches Investigated for Right Ventricular Segmentation Using Short-Axis Cardiac MRI," *IET Image Processing* 15, no. 9 (2021): 1845–1868.

20. M. R. Avendi, A. Kheradvar, and H. Jafarkhani, "Automatic Segmentation of the Right Ventricle From Cardiac MRI Using a Learning-Based Approach," *Magnetic Resonance in Medicine* 78, no. 6 (2017): 2439–2448.

21. W. P. Santamore and L. J. Dell'Italia, "Ventricular Interdependence: Significant Left Ventricular Contributions to Right Ventricular Systolic Function," *Progress in Cardiovascular Diseases* 40, no. 4 (1998): 289–308.

22. C. Yang, D. Tang, I. Haber, T. Geva, and J. Pedro, "In Vivo MRI-Based 3D FSI RV/LV Models for Human Right Ventricle and Patch Design for Potential Computer-Aided Surgery Optimization," *Computers and Structures* 85, no. 11–14 (2007): 988–997.

23. P. Peng, K. Lekadir, A. Gooya, L. Shao, S. E. Petersen, and A. F. Frangi, "A Review of Heart Chamber Segmentation for Structural and Functional Analysis Using Cardiac Magnetic Resonance Imaging," *Magnetic Resonance Materials in Physics, Biology and Medicine* 29 (2016): 155–195.

24. C. Petitjean and J. N. Dacher, "A Review of Segmentation Methods in Short Axis Cardiac MR Images," *Medical Image Analysis* 15, no. 2 (2011): 169–184.

25. C. Petitjean, M. A. Zuluaga, W. Bai, et al., "Right Ventricle Segmentation From Cardiac MRI: A Collation Study," *Medical Image Analysis* 19, no. 1 (2015): 187–202.

26. F. Odille, A. Bustin, S. Liu, et al., "Isotropic 3 D Cardiac Cine MRI Allows Efficient Sparse Segmentation Strategies Based on 3 D Surface

Reconstruction," *Magnetic Resonance in Medicine* 79, no. 5 (2018): 2665–2675.

27. B. Villard, V. Grau, and E. Zacur, "Surface Mesh Reconstruction From Cardiac MRI Contours," *Journal of Imaging* 4, no. 1 (2018): 16.

28. Y. Al Khalil, S. Amirrajab, C. Lorenz, J. Weese, J. Pluim, and M. Breeuwer, "Reducing Segmentation Failures in Cardiac MRI via Late Feature Fusion and GAN-Based Augmentation," *Computers in Biology and Medicine* 161 (2023): 106973.

29. A. Banerjee, E. Zacur, R. P. Choudhury, and V. Grau, "Automated 3D Whole-Heart Mesh Reconstruction From 2D Cine MR Slices Using Statistical Shape Model," (2022), in *IEEE*, 1702–1706.

30. Q. Chang, Z. Yan, M. Zhou, et al., "Deeprecon: Joint 2D Cardiac Segmentation and 3D Volume Reconstruction via a Structure-Specific Generative Method," (2022), in *Springer*, 567–577.

31. M. Sermesant, H. Delingette, H. Cochet, P. Jais, and N. Ayache, "Applications of Artificial Intelligence in Cardiovascular Imaging," *Nature Reviews Cardiology* 18, no. 8 (2021): 600–609.

32. I. Fumagalli, M. Fedele, C. Vergara, et al., "An Image-Based Computational Hemodynamics Study of the Systolic Anterior Motion of the Mitral Valve," *Computers in Biology and Medicine* 123 (2020): 103922.

33. L. Antiga, M. Piccinelli, L. Botti, B. Ene-Iordache, A. Remuzzi, and D. A. Steinman, "An Image-Based Modeling Framework for Patient-Specific Computational Hemodynamics," *Medical and Biological Engineering and Computing* 46 (2008): 1097–1112.

34. M. Fedele and A. Quarteroni, "Polygonal Surface Processing and Mesh Generation Tools for the Numerical Simulation of the Cardiac Function," *International Journal for Numerical Methods in Biomedical Engineering* 37, no. 4 (2021): e3435.

35. S. Klein, M. Staring, K. Murphy, M. A. Viergever, and J. P. Pluim, "Elastix: A Toolbox for Intensity-Based Medical Image Registration," *IEEE Transactions on Medical Imaging* 29, no. 1 (2009): 196–205.

36. P. Thévenaz and M. Unser, "Optimization of Mutual Information for Multiresolution Image Registration," *IEEE Transactions on Image Processing* 9, no. 12 (2000): 2083–2099.

37. J. Lötjönen and T. Mäkelä, "Elastic Matching Using a Deformation Sphere," (2001), in *Springer*, 541–548.

38. H. Lester and S. R. Arridge, "A Survey of Hierarchical Non-linear Medical Image Registration," *Pattern Recognition* 32, no. 1 (1999): 129–149.

39. W. E. Lorensen and H. E. Cline, "Marching Cubes: A High Resolution 3D Surface Construction Algorithm," *ACM Siggraph Computer Graphics* 21, no. 4 (1987): 163–169.

40. J. C. Grignola, "Hemodynamic Assessment of Pulmonary Hypertension," *World Journal of Cardiology* 3, no. 1 (2011): 10–17.

41. A. J. Pappano and W. G. Wier, *Cardiovascular Physiology-E-Book* (United States: Elsevier Health Sciences, 2018).

42. W. Li, K. Wan, Y. Han, et al., "Reference Value of Left and Right Atrial Size and Phasic Function by SSFP CMR at 3.0 T in Healthy Chinese Adults," *Scientific Reports* 7, no. 1 (2017): 3196.

43. N. Kawel-Boehm, S. J. Hetzel, B. Ambale-Venkatesh, et al., "Reference Ranges ('Normal Values') for Cardiovascular Magnetic Resonance (CMR) in Adults and Children: 2020 Update," *Journal of Cardiovascular Magnetic Resonance* 22, no. 1 (2020): 1–63.

44. S. Pujadas, G. P. Reddy, O. Weber, J. J. Lee, and C. B. Higgins, "MR Imaging Assessment of Cardiac Function," *Journal of Magnetic Resonance Imaging* 19, no. 6 (2004): 789–799.

45. S. Kutty, Q. Shang, N. Joseph, et al., "Abnormal Right Atrial Performance in Repaired Tetralogy of Fallot: A CMR Feature Tracking Analysis," *International Journal of Cardiology* 248 (2017): 136–142.

46. S. E. Luijnenburg, R. E. Peters, R. J. van der Geest, et al., "Abnormal Right Atrial and Right Ventricular Diastolic Function Relate to Impaired Clinical Condition in Patients Operated for Tetralogy of Fallot," *International Journal of Cardiology* 167, no. 3 (2013): 833–839.

47. E. Riesenkampff, L. Mengelkamp, M. Mueller, et al., "Integrated Analysis of Atrioventricular Interactions in Tetralogy of Fallot," *American Journal of Physiology–Heart and Circulatory Physiology* 299, no. 2 (2010): H364–H371.

48. L. Bennati, V. Giambruno, F. Renzi, et al., "Turbulence and Blood Washout in Presence of Mitral Regurgitation: A Computational Fluid-Dynamics Study in the Complete Left Heart," (2023), *bioRxiv*, 2023–03.

49. J. P. Bokma, T. Geva, L. A. Sleeper, et al., "A Propensity Score-Adjusted Analysis of Clinical Outcomes After Pulmonary Valve Replacement in Tetralogy of Fallot," *Heart* 104, no. 9 (2018): 738–744.

50. P. E. Ferraz Cavalcanti, M. P. B. O. Sá, C. A. Santos, et al., "Pulmonary Valve Replacement After Operative Repair of Tetralogy of Fallot: Meta-Analysis and Meta-Regression of 3,118 Patients From 48 Studies," *Journal of the American College of Cardiology* 62, no. 23 (2013): 2227–2243.

51. G. Rozzi, F. P. Lo Muzio, L. Fassina, et al., "Right Ventricular Functional Recovery Depends on Timing of Pulmonary Valve Replacement in Tetralogy of Fallot: A Video Kinematic Study," *European Journal of Cardio-Thoracic Surgery* 59, no. 6 (2021): 1329–1336.

52. H. Hu, N. Pan, and A. F. Frangi, "Fully Automatic Initialization and Segmentation of Left and Right Ventricles for Large-Scale Cardiac MRI Using a Deeply Supervised Network and 3D-ASM," *Computer Methods and Programs in Biomedicine* 240 (2023): 107679.

53. A. Quarteroni, A. Manzoni, and C. Vergara, *Mathematical Modelling of the Human Cardiovascular System: Data, Numerical Approximation, Clinical Applications* (United Kingdom: Cambridge University Press, 2019).

54. K. Stein, T. Tezduyar, and R. Benney, "Mesh Moving Techniques for Fluid-Structure Interactions With Large Displacements," *Journal of Applied Mechanics* 70, no. 1 (2003): 58–63.

55. C. Hirt, A. Amsden, and J. Cook, "An Arbitrary Lagrangian–Eulerian Computing Method for All Flow Speeds," *Journal of Computational Physics* 135, no. 2 (1997): 203–216.

56. F. Nobile and L. Formaggia, "A Stability Analysis for the Arbitrary Lagrangian Eulerian Formulation With Finite Elements," *East-West Journal of Numerical Mathematics* 7 (1999): 105–132.

57. M. Fedele, E. Faggiano, L. Dedè, and A. Quarteroni, "A Patient-Specific Aortic Valve Model Based on Moving Resistive Immersed Implicit Surfaces," *Biomechanics and Modeling in Mechanobiology* 16 (2017): 1779–1803.

58. M. A. Fernández, J. F. Gerbeau, and V. Martin, "Numerical Simulation of Blood Flows Through a Porous Interface," *ESAIM. Mathematical Modelling and Numerical Analysis* 42, no. 6 (2008): 961–990.

59. F. Nicoud, H. B. Toda, O. Cabrit, S. Bose, and J. Lee, "Using Singular Values to Build a Subgrid-Scale Model for Large Eddy Simulations," *Physics of Fluids* 23, no. 8 (2011): 085106.

60. S. Katz, A. Caiazzo, B. Moreau, et al., "Impact of Turbulence Modeling on the Simulation of Blood Flow in Aortic Coarctation," (2022), *arXiv preprint*, arXiv:2208.14217.

61. S. Stella, C. Vergara, L. Giovannacci, A. Quarteroni, and G. Prouse, "Assessing the Disturbed Flow and the Transition to Turbulence in the Arteriovenous Fistula," *Journal of Biomechanical Engineering* 141, no. 10 (2019): 101010.

62. C. Vergara, D. Le Van, M. Quadrio, L. Formaggia, and M. Domanin, "Large Eddy Simulations of Blood Dynamics in Abdominal Aortic Aneurysms," *Medical Engineering and Physics* 47 (2017): 38–46.

63. P. C. Africa, I. Fumagalli, M. Bucelli, et al., "-lifex-cfd: An Open-Source Computational Fluid Dynamics Solver for Cardiovascular Applications," *Computer Physics Communications* 296 (2024): 109039, https://doi.org/10.1016/j.cpc.2023.109039.

64. H. Jasak and Z. Tukovic, "Automatic Mesh Motion for the Unstructured Finite Volume Method," *Transactions of FAMENA* 30, no. 2 (2006): 1–20.

65. P. C. Africa, "lifex: A Flexible, High Performance Library for the Numerical Solution of Complex Finite Element Problems," *SoftwareX* 20 (2022): 101252.

66. T. E. Tezduyar and M. Senga, "Stabilization and Shock-Capturing Parameters in SUPG Formulation of Compressible Flows," *Computer Methods in Applied Mechanics and Engineering* 195, no. 13–16 (2006): 1621–1632.

67. K. Yared, P. Noseworthy, A. E. Weyman, E. McCabe, M. H. Picard, and A. L. Baggish, "Pulmonary Artery Acceleration Time Provides an Accurate Estimate of Systolic Pulmonary Arterial Pressure During Transthoracic Echocardiography," *Journal of the American Society of Echocardiography* 24, no. 6 (2011): 687–692.

68. 123sonography, "Pulmonary Acceleration Time to Estimate Pulmonary Pressure," (2023), https://123sonography.com/ebook/pulmonary-acceleration-time-to-estimate-pulmonary-pressure.

69. MSDManuals, "Normal Pressures in the Heart and Great Vessels," (2023), Values Adapted From Fowler No: Cardiac Diagnosis and Treatment, ed. 3, Philadelphia, JB Lippincott, 1980, 11, https://www.msdmanuals.com/professional/multimedia/table/normal-pressures-in-the-heart-and-great-vessels.